



Understanding ozone episodes during the TRACER-AQ campaign in Houston, Texas: The role of transport and ozone production sensitivity to precursors



Ehsan Soleimanian ^a, Yuxuan Wang ^{a,*}, Wei Li ^a, Xueying Liu ^a, Travis Griggs ^a, James Flynn ^a, Paul J. Walter ^b, Mark J. Estes ^b

^a Department of Earth and Atmospheric Sciences, University of Houston, Houston 77204, TX, USA

^b Department of Mathematics, St. Edward's University, Austin 78704, TX, USA

ARTICLE INFO

Editor: Hai Guo

Keywords:

TRACER-AQ

Houston

Ozone formation tendency

CAMx

FLEXPART

ABSTRACT

This study investigated transport pathways and photochemical formation responsible for ozone exceedances during the September 2021 deployment of the Tracking Aerosol Convection Interactions ExpeRiment/Air Quality (TRACER-AQ) campaign in Houston, Texas. We focused on two ozone episodes, September 6th–September 11th (“Episode 1”) and September 23rd–September 26th (“Episode 2”), when the maximum daily eight-hour average (MDA8) ozone at surface monitors exceeded 70 ppbv. Long-range transport patterns of air masses during these episodes were from the central/northern US. High-resolution (4 km resolution) trajectory analysis with FLEXible PARTicle (FLEXPART) dispersion model revealed local recirculation of air masses and the accumulation of pollutants across Houston contribute to the ozone exceedances. Comprehensive Air Quality Model with extensions (CAMx) driven by 1.33-km resolution meteorology from the Weather Research and Forecast (WRF) tool simulated elevated ozone production rates during ozone episodes across the Houston metropolitan area, with ozone production hotspots mostly over Houston city and industrial districts of the Houston Ship Channel (HSC). The regional increase in ozone production rates was due to the transport of VOC-rich air masses (via northerly flows) that brought ozone precursors to the region, which ultimately caused a transition in the ozone formation tendency from generally VOC-limited to NO_x-limited conditions. However, the city of Houston and the HSC remained in a VOC-limited regime because of local NO_x emissions that, to some extent, preponderated the impact of transported VOCs. While approximately 37 % of the elevated ozone production was attributed to local photochemistry, the remaining ~63 % increase in ozone production was due to the transported ozone to the region during episodes, bringing ozone to the Houston region and contributing to ozone exceedances. The outcomes of this study illustrated the synergy between transport and ozone production, both long-range and local scale, which resulted in ozone exceedances in Houston.

1. Introduction

Tropospheric ozone is recognized as a criteria air pollutant by the U.S. Environmental Protection Agency (EPA) because of its adverse effects on human health (Anenberg et al., 2009; Lefohn et al., 2018). Ozone formation is a function of its precursors (i.e., nitrogen oxides (NO_x) and volatile organic compounds (VOCs)), atmospheric photochemistry, and meteorology (Lu et al., 2019; Wang et al., 2017). Due to the non-linear response of ozone to precursor emissions, ozone production tendency is classified as NO_x-limited or VOC-limited based on the availability of

ozone precursors and physicochemical conditions of the atmosphere. Earlier studies conducted in various regions, such as the U.S. and China, have shown that ozone formation is typically NO_x-limited in continental, remote, and suburban areas, whereas it might be independent of NO_x (i.e., VOC-limited) in urban and industrialized regions (Kleiman et al., 2001; Nuvolone et al., 2018; Tan et al., 2018; Wang et al., 2009). Besides precursor emissions, meteorological factors can enhance or suppress ozone production, imposing challenges in accurately predicting and modeling atmospheric ozone levels (Camalier et al., 2007; Gorai et al., 2015; Yang et al., 2019). In addition, meteorological conditions control

* Corresponding author.

E-mail address: ywang246@central.uh.edu (Y. Wang).

the dynamic transport and mixing of ozone and its precursors on different spatial and temporal scales (Auvray and Bey, 2005; Hidy, 2000). Given the complexity in tropospheric ozone formation and transport, relevant control strategies require a comprehensive understanding of ozone response to NO_x and VOC emissions and how this response would change under different meteorological conditions and various emission sources (Erickson et al., 2020; Jiménez and Baldasano, 2004).

Numerical simulations using Eulerian and Lagrangian approaches have been used in understanding the complex relationship between meteorology, emissions, and atmospheric levels of pollutants. These simulations can describe the physiochemical processes that occur in the atmosphere across various scales, making them appropriate for research studies, regulatory analysis, attainment demonstrations, and decision-making (Daly and Zannetti, 2007; Zannetti, 2013). The Comprehensive Air Quality Model with extensions (CAMx) is a photochemical tool for simulating reaction process of ozone and the sensitivity of ozone-NO_x-VOCs (ENVIRON, 2020). Several studies have employed CAMx to model ozone formation, its sensitivity to precursors, and ozone sources across the U.S., Europe, and east Asia (Du et al., 2022; Krüger et al., 2008; Li et al., 2016; Li et al., 2012; Shu et al., 2023; Wang et al., 2009). For example, Wang et al. (2009), Li et al. (2012), and Li et al. (2016) employed CAMx to determine the chemical and transport mechanisms responsible for ozone pollution events in China. Using the same tool, Krüger et al. (2008) modeled the current and future perspective of ozone formation in Europe in a changing climate. By discerning the contributions of intercontinental transport and domestic emissions to ozone and simulating ozone formation under different production regimes, CAMx has also been used as a robust model to evaluate the impact of emission controls and help guide control policies for ozone (Ge et al., 2021b; Li et al., 2019; Wu et al., 2021; Zhao et al., 2022). While the versatility and applicability of CAMx make it a powerful tool in understanding and addressing air pollution issues, it is challenging to determine the transport of pollutants from emission sources to a receptor using the gridded model. Trajectory tools such as FLEXible PARTicle (FLEXPART) dispersion model can simulate source-receptor dispersion of a plume by Lagrangian tracking of air masses (Pisso et al., 2019; Stohl et al., 1998); however, they have inherent limitations in representing concentration gradients within the atmospheric chemical field. To overcome this limitation, the “folded retroplume” technique, proposed by Owen and Honrath (2009), integrates information from both Eulerian and Lagrangian models, which allows the retrieval of some of the Lagrangian information that is lost during the calculation of gridded Eulerian fields. By overlapping a Eulerian forward simulation with a Lagrangian backward simulation (initiated from the receptor), this method reveals physical and chemical processes occurring throughout the transport. Following this approach, Zhang et al. (2014) convolved the outputs of GEOS-Chem with FLEXPART and modeled ozone production tendency on a regional scale along the transport pathway of North American outflow. Therefore, a semi-Lagrangian perspective on plume aging during transport provides valuable insights into ozone formation, particularly within complex physiochemical scenarios.

The Houston metropolitan area has historically experienced high ozone concentrations and is classified as a “moderate” non-attainment region under the 2015 8-h ozone national ambient air quality standards (NAAQS). Ozone exceedances in the Houston area have been dominantly attributed to various emission sources, such as petrochemical complexes, on-road/off-road vehicles, and industries emitting ozone precursors into the atmosphere (Vizuete et al., 2008; Webster et al., 2007). Houston lies within a unique climate regime where mesoscale and synoptic circulations interact with local emissions, further degrading air quality in the area. Because of the proximity of Houston to the Gulf of Mexico, local land-sea breeze circulations participate in the recirculation of air masses and lead to the accumulation of pollutants in the region (Banta et al., 2005; Li et al., 2020). On the regional scale, up to 60–70 % of surface ozone in the Houston area is estimated to

originally form outside of the region (known as regional background ozone) and is transported to the region under certain synoptic-scale circulation patterns (Langford et al., 2009; Soleimanian et al., 2022). Ozone pollution events in Houston typically start with synoptic-scale northerly and easterly flows transporting pollutants to the area, followed by a sea breeze or stagnant conditions leading to the recirculation and accumulation of pollutants over the land (Li et al., 2020; Loughner et al., 2014; Mazzuca et al., 2017). These ozone level exceedances seasonally peak in late spring and late summer/early fall (Bernier et al., 2019; Wang et al., 2016), making those times suitable opportunities for air quality measurement campaigns.

Extensive field campaigns have been conducted in the Houston area during the last two decades to investigate ozone chemistry and provide knowledge for legislating efficient control strategies. The Texas Air Quality Study in 2000 (TexAQS, 2000) and Texas Air Quality Study II in 2006 (TexAQS, 2006) investigated the chemical and meteorological processes contributing to high ozone levels in Southeast Texas and helped inform the State Implementation Plan (SIP) for ozone reduction (Cowling et al., 2007). The Deriving Information on Surface Conditions from Column and Vertically Resolved Observations Relevant to Air Quality (DISCOVER-AQ, 2013) field campaign in 2013 tried to relate satellite column observations to surface-level ozone for better air quality forecasting through a more accurate understanding of pollutant levels and fluctuations in their emissions. A common finding of the DISCOVER-AQ and TexAQS studies was that ozone formation was mostly VOC-limited in urban and industrialized areas of Houston during rapid ozone formation conditions, while areas farther from Houston were primarily in NO_x-limited and transition regimes (Mazzuca et al., 2016; Zhou et al., 2014). The more recent Tracking Aerosol Convection Interactions ExpeRiment/Air Quality (TRACER-AQ) field campaign was a collaborative interagency effort in the Houston area during September 2021 funded by the Department of Energy (DOE) Atmospheric Radiation Measurement (ARM) user facility, NASA’s Tropospheric Composition Research Program, and the Texas Commission on Environmental Quality (TCEQ). Ambient air quality measurements were collected from various platforms, including aircraft, boats, and ground-based stationary and mobile laboratories, to provide spatial and temporal variations in ozone and its precursors across the Houston area. The main goal of the TRACER-AQ campaign was to characterize the heterogeneous distribution of emissions (along the Houston Ship Channel, Galveston Bay, and the nearby industrial sectors) and their interaction with mesoscale dynamic processes.

To link Houston air quality with emissions, chemistry, and meteorological patterns during the TRACER-AQ campaign, this study focused on ozone production and the chemical evolution of ozone precursors across the Houston area and along their transport pathways. To this end, backward trajectory analyses were conducted to determine the source regions and transport pathways of air masses arriving in the Houston area. These trajectories were then used to sample chemical fields and ozone production/loss rates simulated by a 3-dimensional photochemical model to investigate ozone production and chemical regimes. By combining the simulated chemical fields with the modeled transport pathway of air masses, we defined a semi-Lagrangian framework to investigate the photochemical evolution of pollutants throughout the transport pathway. This approach enabled us to comprehensively investigate ozone chemistry as well as the transport of ozone and its precursors to the Houston area during the TRACER-AQ field campaign period.

2. Methodology

2.1. Study area and surface ozone data

The Texas Commission on Environmental Quality (TCEQ) air monitoring network consists of several monitoring stations across the greater Houston area measuring levels of surface pollutants. Fig. 1 shows the

Table 1

Summary of the mean values for ozone formation rates, levels of ozone precursors, and OH loss/HO₂ production rates for the entire d03 domain as well as the corresponding values over the Southeast Houston, HSC, and Galveston Bay regions (shown in bold – corresponding to the white rectangles in Fig. 4, Fig. 5, Fig. 7, Fig. 8, and Fig. 9).

Parameter (unit)	Non-episode days	Episode 1	Episode 2
Fig. 4			
Net PO ₃ (ppb/h)	-0.11 ± 6.90	1.70 ± 6.21	1.50 ± 6.02
	-1.89 ± 14.08	1.99 ± 13.51	1.32 ± 13.25
VOC-limited PO ₃ (ppb/h)	0.28 ± 1.64	0.17 ± 1.52	0.23 ± 1.39
	0.65 ± 2.19	0.63 ± 2.78	0.85 ± 2.36
NO _x -limited PO ₃ (ppb/h)	0.81 ± 1.62	1.92 ± 2.02	1.65 ± 1.46
	1.01 ± 2.00	2.86 ± 2.98	2.04 ± 1.91
Fig. 5			
L _N /Q	1.00 ± 1.37	0.23 ± 0.27	0.32 ± 0.33
	1.69 ± 1.99	0.41 ± 0.49	0.54 ± 0.53
Fig. 7			
NO _x (ppbv)	1.24 ± 1.93	0.74 ± 1.22	0.75 ± 1.16
	2.45 ± 3.23	1.48 ± 2.50	1.56 ± 2.17
PAN (ppbv)	0.14 ± 0.19	0.36 ± 0.32	0.43 ± 0.29
	0.17 ± 0.19	0.53 ± 0.43	0.61 ± 0.35
Fig. 8			
Paraffins (ppbv)	9.44 ± 7.34	20.49 ± 8.82	13.52 ± 5.93
	12.50 ± 8.49	24.46 ± 10.06	17.72 ± 6.83
Olefins (ppbv)	0.13 ± 0.21	0.09 ± 0.12	0.07 ± 0.09
	0.21 ± 0.28	0.15 ± 0.14	0.11 ± 0.12
Aromatics (ppbv)	0.17 ± 0.29	0.24 ± 0.21	0.17 ± 0.18
	0.31 ± 0.43	0.38 ± 0.26	0.29 ± 0.25
Biogenic VOCs (ppbv)	1.11 ± 2.40	0.64 ± 0.85	0.46 ± 0.60
	1.35 ± 1.83	0.82 ± 0.75	0.55 ± 0.48
Aldehydes (ppbv)	1.95 ± 1.36	3.78 ± 1.80	2.55 ± 0.99
	2.29 ± 1.33	4.53 ± 1.69	0.39 ± 0.51
Ketones (ppbv)	0.98 ± 0.76	2.57 ± 1.12	1.50 ± 0.72
	1.12 ± 0.78	2.77 ± 1.29	0.72 ± 0.80
Fig. 9			
OH loss (ppb/h)	1.21 ± 1.43	2.42 ± 1.54	1.75 ± 1.24
	1.89 ± 1.87	3.74 ± 2.21	2.78 ± 1.61
HO ₂ production (ppb/h)	2.48 ± 2.55	5.56 ± 2.73	4.15 ± 2.06
	3.43 ± 3.29	7.70 ± 3.86	5.75 ± 2.72

map of selected sites within the study area, including Aldine, Haden Road, Lynchburg Ferry, Bayland Park, Manvel Croix Park, and Galveston. These selected sites are representative of various land uses (e.g., industrial, commercial, and residential) within urban and suburban

districts. The Aldine station is located in a suburban region approximately 18 km north of the urban Houston area. The Haden Road and Lynchburg Ferry sites are in close proximity to the Houston Ship Channel (HSC) and highly exposed to emissions from petrochemical and industrial plants. Bayland Park is ~15 km southwest of downtown Houston within a commercial/residential land use. The suburban area of Manvel Croix Park and the coastal region of Galveston sites are ~25 km and ~70 km south of Houston city, respectively. Hourly surface ozone levels for the selected sites during the TRACER-AQ campaign (i.e., September 2021) were downloaded from the Texas Air Monitoring Information System (TAMIS) database and had, on average, ~90 % completeness within the investigation period. The surface ozone data were used to identify periods with elevated ozone levels (hereafter, “ozone episodes”) across the study area during the TRACER-AQ campaign. Similarly, we obtained hourly data for meteorological parameters, such as temperature and wind speed, as well as NO_x and selected VOCs (including ethane, propane, benzene, and toluene) from the TAMIS database. The measurements of NO_x were conducted using Model 42 gas-phase chemiluminescent monitors (Thermo Environmental Instruments Inc., Franklin, MA, USA), which have been designated as a federally recognized method (RFNA-1289-074) by the US Environmental Protection Agency (EPA) under 40 CFR Part 53. In this method, ambient air passes through a heated catalyst to convert nitrogen dioxide (NO₂) into nitrogen oxides (NO). The reaction of NO with oxygen and the subsequent decay of excited NO₂ to the ground state result in the emission of infrared radiation, which is proportional to the concentration of reacted NO. Levels of VOCs were also measured by TCEQ using a continuous preconcentration trap system (PE 8700) coupled with an automated gas chromatograph (GC) equipped with a dual flame ionization detector (FID). It is worth noting that VOC measurements were available only at the Lynchburg Ferry and Haden Road sites. These surface measurements at the monitoring sites were used for evaluating the performance of the model.

2.2. Overview of multi-scale photochemical modeling and trajectory analysis

Air quality challenges in the Houston area are related to complex local and regional meteorological conditions coupled with unique industrial emissions (Banta et al., 2005). To capture the meteorological complexity, we employed the Weather Research and Forecasting (WRF)

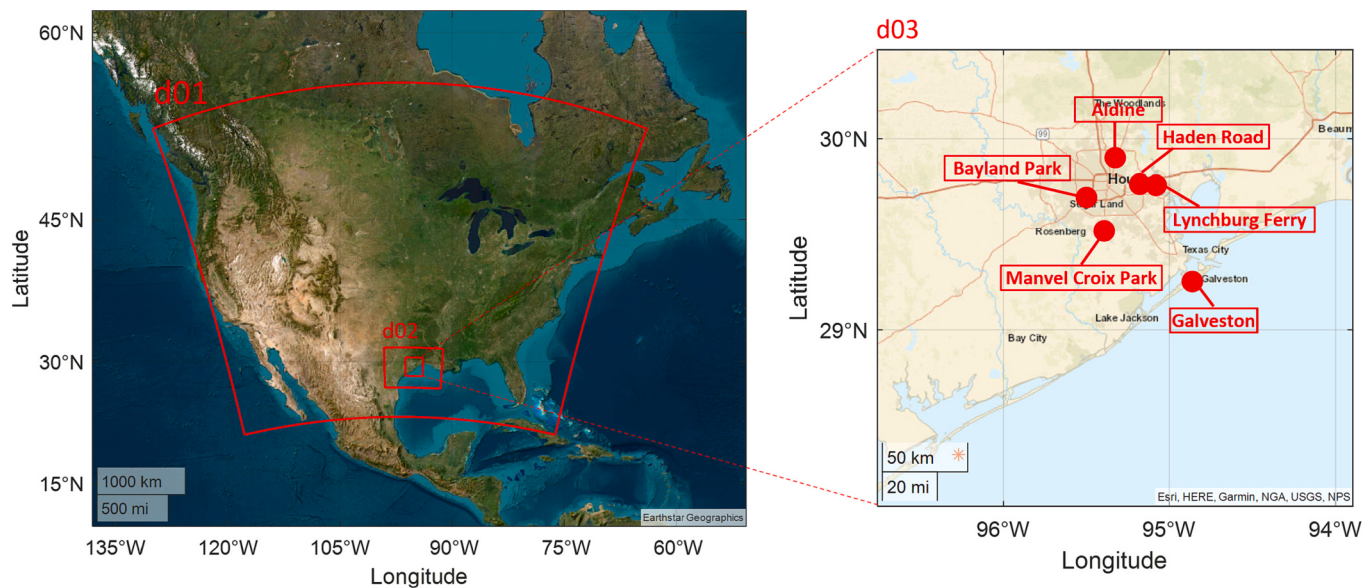


Fig. 1. Map of the WRF-CAMx domains (left) and the selected monitoring sites across the Houston-Galveston region (right). The three domains cover the contiguous United States (d01), Southeast Texas (d02), and the Houston-Galveston region (d03).

model to simulate meteorological fields for three domains over the contiguous United States, Southeast Texas, and the Houston-Galveston-Brazoria region with increasing horizontal resolutions, shown as d01, d02, and d03 respectively in Fig. 1. Using the WRF-generated meteorological fields, 3-dimensional backward trajectory analysis was performed using the Hybrid Single-Particle Lagrangian Integrated Trajectory (HYSPLIT) model and FLEXible PARTicle (FLEXPART) dispersion model to track the pathway and dispersion of air masses transporting pollutants to the Houston area during the TRACER-AQ campaign. The HYSPLIT model was used to derive regional-scale transport patterns using coarse resolution (12 km) meteorological fields, while the FLEXPART model was employed to simulate local-scale (4 km) plume dispersion (backward in time). Since backward trajectory analysis in FLEXPART accounts for parameterization of sub-grid-scale turbulence and convective processes, whereas HYSPLIT does not, the former simulates small-scale atmospheric variability that affects particle dispersion (Verreyken et al., 2019). Therefore, FLEXPART better represents complex local-scale processes that govern atmospheric transport patterns. In the next step, the Comprehensive Air quality Model with extensions (CAMx) was employed using the WRF-simulated meteorology to model 3-dimensional chemical fields over the study domains. The CAMx outputs include 3-D distributions of ozone and its precursors (i.e., NO_x and speciated VOCs) along with ozone production rates by different chemical pathways. Finally, a semi-Lagrangian framework was defined by coupling FLEXPART dispersed plumes with CAMx-generated chemical fields in which the levels of different pollutants and ozone production rates from CAMx were sampled along the path of air parcels derived from the FLEXPART model. This approach enabled us to investigate the photochemical evolution of pollutants throughout the transport pathway. Further details and configurations regarding the WRF, CAMx, HYSPLIT, and FLEXPART models are discussed in the following subsections.

2.2.1. WRF model configurations

The WRF model is an atmospheric mesoscale numerical weather prediction tool developed for weather forecasting and atmospheric research needs (Skamarock et al., 2019; Skamarock et al., 2008). In this study, we used WRF version 3.9.1.1 with the Advanced Research WRF (ARW) solver to simulate meteorological fields for three domains (as shown in Fig. 1) with a horizontal grid spacing of 12 km × 12 km, 4 km × 4 km, and 1.33 km × 1.33 km, respectively. All three domains consisted of 45 vertical levels in the native model grid (eta levels) extending from the surface to the 50 hPa pressure level. The selected configurations in the WRF-ARW model include the local closure Mellor-Yamada-Nakanishi-Niino (MYNN) planetary boundary layer (PBL) scheme (Nakanishi and Niino, 2009), Morrison double moment (2 M) micro-physics scheme (Morrison et al., 2009), Rapid Radiative Transfer Model (RRRTMG) longwave and shortwave radiation schemes (Iacono et al., 2008), Monin-Obukhov similarity surface layer scheme (Chen et al., 1997), Noah land-surface module (Chen and Dudhia, 2001), and the New Tiedtke cumulus parameterization for sub-grid-scale effects of clouds (Tiedtke, 1989; Zhang et al., 2011). The initial and meteorological boundary conditions were generated from the outer domain to the inner domain, except for d01, which got boundary conditions from the National Centers for Environmental Prediction (NCEP)-Final Analysis (FNL) global analysis at 0.25° × 0.25° resolution. Lastly, the WRF simulations were nudged using the observed temperature, relative humidity, and wind data recorded at the TCEQ continuous ambient monitoring stations (CAMS). It has been reported that nudging can improve WRF simulations by constraining the model through an artificial forcing to be more consistent with observations (Glisan et al., 2013; Liu et al., 2012). The details of WRF modeling settings for the TRACER-AQ period are presented by Liu et al. (2023).

2.2.2. CAMx photochemical modeling

CAMx is an open-access photochemical model that can simulate

emissions, chemical reactions, dispersion, and removal of pollutants in the atmosphere from local to continental scales (ENVIRON, 2020). This tool solves the 3-dimensional Eulerian continuity equation based on the “one atmosphere” framework for different chemical species to model their distribution over a defined domain. CAMx is the regulatory model suggested by TCEQ to simulate pollutants concentrations and their sensitivities to various state control policies. In this study, we applied CAMx version 7.10 over the contiguous United States, Southeast Texas, and the Houston-Galveston-Brazoria region (as shown in Fig. 1) during September 2021. The model requires gridded input of meteorology and emissions to simulate the chemical fields. We ran CAMx on the three domains similar to WRF that share the same Lambert Conformal Conic projection. The WRF meteorological outputs were translated into a CAMx-friendly format using the WRF-CAMx version 5.1 pre-processor tool. To alleviate the CAMx computational costs, WRF vertical layers were collapsed into 30 unevenly distributed levels with a higher resolution near the surface that extend up to ~11 km (100 hPa) above the ground level (AGL). We used the emission data from the 2019 State Implementation Plan (SIP) modeling platform provided by TCEQ after cropping the gridded data (to match the boundaries of our CAMx simulations) and re-distributing the emissions from 4 km resolution to a finer resolution of 1.33 km over the Houston area, as described in Li et al. (2023).

The CAMx simulation was operated with a spin-up period of 10 days to minimize the effects of initial and boundary conditions. The initial and boundary conditions for the 12-km domain were obtained from the GEOS-Chem (version 12.2.1) global simulation with emissions from the 2011 National Emission Inventory (NEI) scaled to 2019, whereas those for 4 km and 1.33 km domains were extracted from the hourly CAMx simulation outputs of 12 km and 4 km resolution, respectively. Spatio-temporal variations in the levels of atmospheric pollutants are resulted from complicated interactions between various atmospheric processes, including chemical processes, transport, and deposition (Shen et al., 2011; X. Wang et al., 2010). The chemical process analysis (CPA) probing tool was enabled to provide detailed information on the chemical processes during model simulations. This tool incorporates the Integrated Process Rate (IPR) analysis embedded in CAMx, which helps estimate the contributions of major physical and chemical processes to the formation and accumulation of a target species. The IPR analysis examines the temporal variations in the contributions from gas-phase chemistry, transport (both advection and diffusion), and deposition, while at the same time, offering the flexibility to be used over a region with specified vertical layers (Huang et al., 2016; Shen et al., 2011). In this work, we focused on the lowest five layers (AGL < 500 m) over the d03 domain in the CAMx simulations to investigate the processes occurring from the surface to the mid-PBL.

2.2.3. HYSPLIT backward trajectory analysis

Lagrangian models simulate the atmospheric transport and dispersion of pollutants from an emission source (forward modeling) or to a receptor (backward modeling) (Han et al., 2005; Hegarty et al., 2013). The HYSPLIT trajectory model is developed by the National Oceanic and Atmospheric Administration (NOAA) Air Resources Laboratory (ARL) and has been widely used to model the transport pattern of various atmospheric pollutants (Stein et al., 2015). This model derives the movement of an air parcel based on the advection of a single particle via a mean 3-dimensional velocity field (Draxler and Rolph, 2010). In this study, we employed HYSPLIT version 5.2.0 for backward trajectory analyses to model the transport pathway of pollutants to the Houston region during the TRACER-AQ campaign. The HYSPLIT model was driven using the North American Mesoscale (NAM) regional analysis fields to determine the long-range transport of air masses to the Houston region. The NAM wind field is maintained by NCEP over the contiguous United States and is available online at NOAA's database with 12 km horizontal resolution, 27 vertical pressure levels (from surface to 50 hPa), and a temporal resolution of 3 h. Hourly back trajectories were

started for a duration of 72 h from endpoints at 200 m and 2000 m AGL at the Lynchburg Ferry station. This site was chosen as the receptor for trajectory analysis due to its proximity to the HSC, a significant emission source of VOCs and NO_x in the Houston area. Previous studies (as well as the current work, as will be discussed in Section 3.3) have reported enhanced ozone production rates in this region during pollution events, making it an ideal location for studying the transport of precursors and their influence on ozone formation (Mazzuca et al., 2016; Zhou et al., 2014). The receptor at 200 m AGL was selected to represent the well-mixed conditions in the boundary layer, while the 2000 m one can be associated with ozone in free troposphere. The generated hourly trajectories for September 2021 were used as the input to Ward's agglomerative hierarchical clustering algorithm included in the HYSPLIT package. This iterative process begins with assigning each trajectory to a cluster and continues by merging different clusters while minimizing the spatial differences between trajectories within a cluster (Stein et al., 2015; Ward Jr, 1963).

While the 72-h back trajectories from HYSPLIT are informative in identifying the pollution episodes and long-range transport pathways of pollutants, we also generated higher-resolution (4 km) daily-integrated trajectories to provide insight into the local-scale transport pattern of pollutants across the Houston region. Previous studies have shown that high-resolution WRF meteorological fields can more accurately simulate horizontal temperature gradients at land-water intercepts than NAM, better capturing mesoscale transport patterns (Kotsakis et al., 2022; Loughner et al., 2011). Thus, we ran HYSPLIT using the WRF-simulated meteorological fields from the d02 domain (4 km × 4 km resolution) to model the local-scale transport pattern of air masses across Southeast Texas during the TRACER-AQ campaign. The model configurations followed those of long-range transport analysis, and the simulation was terminated when an air parcel left the geographical limits of the meteorological domain (i.e., d02). In a single trajectory analysis with no vertical turbulence, the released air parcel may hit the ground and lose information about the vertical motion. To avoid this shortcoming of the HYSPLIT model, trajectories were stopped when air parcels reached relatively close to the ground level (altitude <10 m AGL).

2.2.4. FLEXPART model and plume history analysis

FLEXPART is a Lagrangian particle dispersion model designed for simulating the synoptic and mesoscale transport of air pollutants (Pisso et al., 2019; Stohl et al., 1998). This model computes both forward and backward stochastic dispersion and transport pathways for a large number of air parcels relative to a starting point. When used in the backward mode, FLEXPART resolves the spatial distribution of air parcels (hereafter, "retroplume") emitted from the receptor and advected/dispersed backward in time. While HYSPLIT backward trajectories are based on the 3-dimensional advection field, FLEXPART accounts for 3-D convection and turbulence of the air masses. The convection is parametrized by the Zivkovic-Rothman scheme (Emanuel and Živković-Rothman, 1999) and the Hanna scheme (Hanna, 1982) with skewed turbulence in the convective boundary layer is assumed for the turbulence. Moreover, the model considers both the skewness of turbulence in the vertical velocity as well as the vertical gradient in the air density, which makes it a powerful tool for analyzing the stochastic dispersion of air masses (Pisso et al., 2019; Stohl et al., 2005; Verreyken et al., 2019).

To better describe the source-receptor relationship and transformation of pollutants along the retroplume, it is suggested to convolve the outputs from backward trajectory analysis for each release by the chemical fields of interest computed from a forward simulation as shown in Eq. (1) (Owen and Honrath, 2009; Zhang et al., 2014):

$$M_t = \frac{\sum_i f(P_{i,t}) \bullet X_t}{p_t} \quad (1)$$

where M_t is the folded retroplume at time t along the trajectory pathway, p_t refers to the number of particles, and X_t is the CAMx-simulated 3-

dimensional chemical field for a parameter of interest (e.g., ozone level, ozone production rate, etc.). $P_{i,t}$ denotes the location of the i^{th} air parcel, and $f(P_{i,t})$ generates a null matrix with exactly the same shape as X_t in which the element that corresponds to the closest gridline in $P_{i,t}$'s geographical location is set to unity. Lastly, the mean M_t throughout the trajectory provides an estimate of a specific parameter over the entire dispersed plume. This approach builds a semi-Lagrangian framework to sample air masses along the trajectory pathway from an Eulerian CAMx field that simulates the chemical transformation of pollutants, allowing for the analysis of complex transport scenarios.

In this study, we employed FLEXPART-WRF version 3.1 developed by Brioude et al. (2013) to directly use WRF-generated meteorological fields (i.e., d02) into FLEXPART. While HYSPLIT derived daily integrated transport patterns of single air parcels during ozone episodes, FLEXPART was used to simulate plume dispersion, focusing on afternoon hours when ozone levels peak. Thus, FLEXPART was run in backward mode during ozone episodes by releasing 1000 passive tracers within 12 PM – 3 PM local time at surface level (5 m – 15 m AGL) from Lynchburg Ferry. The release time was set at 12 PM – 3 PM to coincide with the afternoon ozone peak, as also observed in previous studies within the region (Morris et al., 2010). Lastly, the backward trajectory analysis was run for a duration of 24 h as long as >500 air parcels remained within the geographical limits of the meteorological field (d02).

3. Results and discussions

3.1. Identifying ozone episodes and WRF-CAMx evaluations

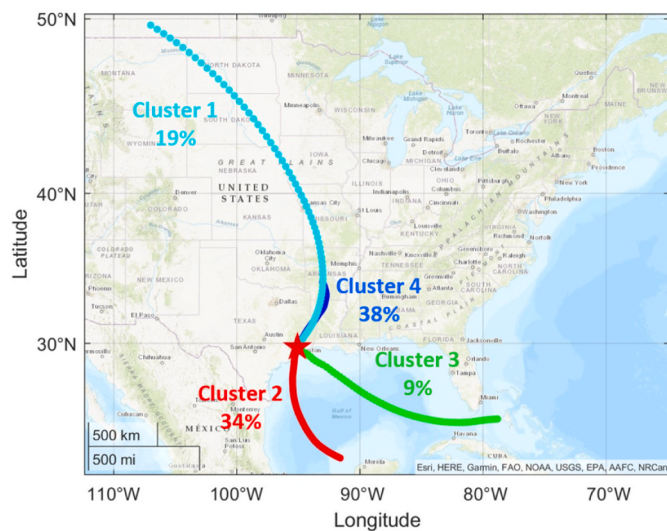
Surface levels of ozone were analyzed across the selected TCEQ monitoring sites (i.e., Aldine, Haden Road, Lynchburg Ferry, Bayland Park, Manvel Croix Park, and Galveston) to capture spatial and temporal variations in ozone during September 2021. Ozone episodes were identified when the maximum daily eight-hour average (MDA8) ozone at a monitoring site exceeded the NAAQS-2015 standard of 70 ppbv (Federal Register, 2015). "Episode 1" was selected as September 6th – September 11th, during which high MDA8 ozone levels (within the range of 71 ppbv – 89 ppbv) were recorded across the selected sites. Similarly, September 23rd – September 26th was identified as "Episode 2" when MDA8 ozone levels were slightly higher than the threshold of 70 ppbv (within the range of 71 ppbv – 73 ppbv). Averaged across the selected sites, hourly levels of ozone increased by ~88 % and ~75 %, respectively, during Episode 1 (39.8 ± 20.1 ppbv) and Episode 2 (37.0 ± 21.5 ppbv), compared with non-episode days (21.1 ± 10.6 ppbv) during September 2021 (Fig. S1). Elevated levels of hourly ozone (28.5 ± 18.3 ppbv) were also observed from September 17th – September 19th, most probably due to the remnants of Hurricane Nicholas meandering over the region (Latto et al., 2021). Since the study of Hurricane Nicholas and its impacts on ozone levels were beyond the scope of the current work, the September 17th – September 19th episode is not analyzed in this study. The surface meteorological parameters measured at the selected TCEQ sites revealed that Episode 1 had relatively similar temperature (27.2 ± 0.73 °C) and wind speed (2.23 ± 0.54 m/s) compared with non-episode days (26.5 ± 3.40 °C, 2.73 ± 1.24 m/s). Episode 2 was approximately 4 °C colder (i.e., 22.5 ± 0.79 °C) and wind speed (1.87 ± 0.30 m/s) dropped by ~34 % compared with non-episode days.

While a comprehensive assessment of the WRF and CAMx models against TRACER-AQ observations has been reported in Liu et al. (2023) and Li et al. (2023), we have performed an evaluation of the WRF-CAMx model using surface measurements obtained from the selected TCEQ sites. The statistical metrics used for model evaluation and summary statistics of the WRF-CAMx model performance are presented in Table S1 and Table S2, respectively. The evaluation of 24-h modeled ozone levels against surface measurements (Fig. S2 and Fig. S3) revealed

that the model well-captured the variations ($R = 0.85$) but overestimated ozone levels by 8.94 ppbv (~33%). Furthermore, the mean error during non-episode days was 9.32 ppb, while it was 8.76 ppb during ozone episodes, indicating a 45% and 23% overestimation of ozone levels, respectively. Evaluating the model performance for predicting meteorological parameters, NO_x , and selected VOC levels (Fig. S2 and Fig. S3), we found that the model exhibited a 93% capture

of variability in surface temperature with a slight overestimation of 0.23°C (~1%). For wind speed, the model captured 62% of the variability but overestimated it by 0.73 m/s (~32%), which is a common problem in WRF. The model captured 50% of the variability while overestimating NO_x levels by 40%. Furthermore, the model successfully captured 52%–60% of the variability in the selected VOCs. However, there were variations in the accuracy of the model predictions, with

(a)



(b)

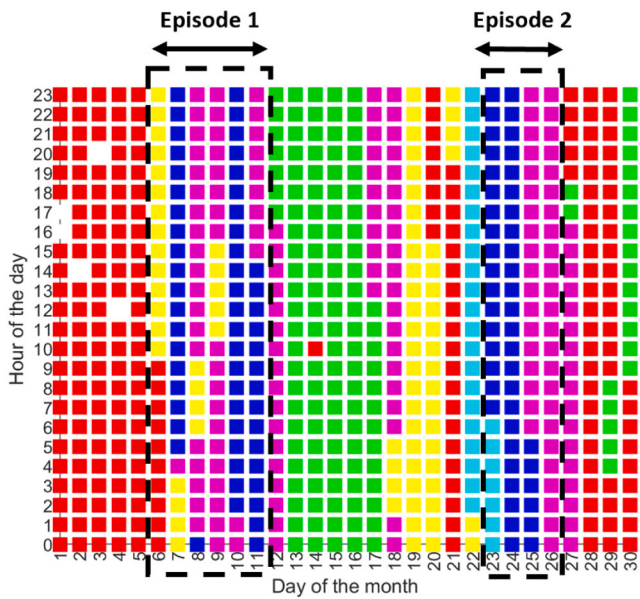
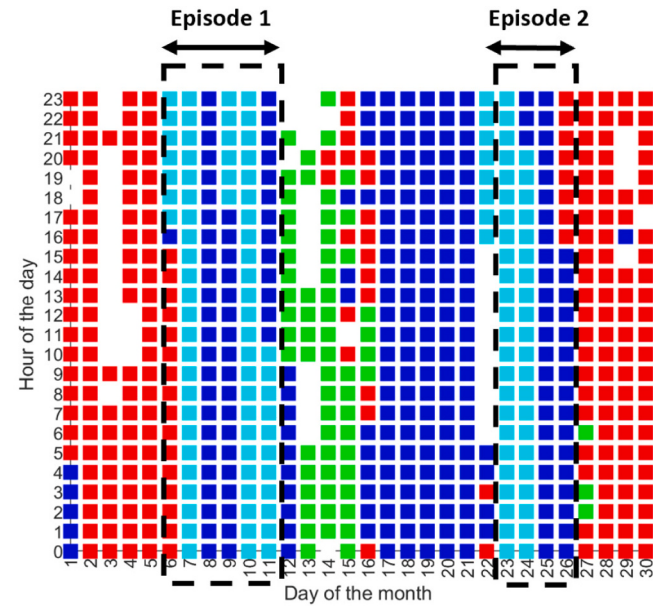
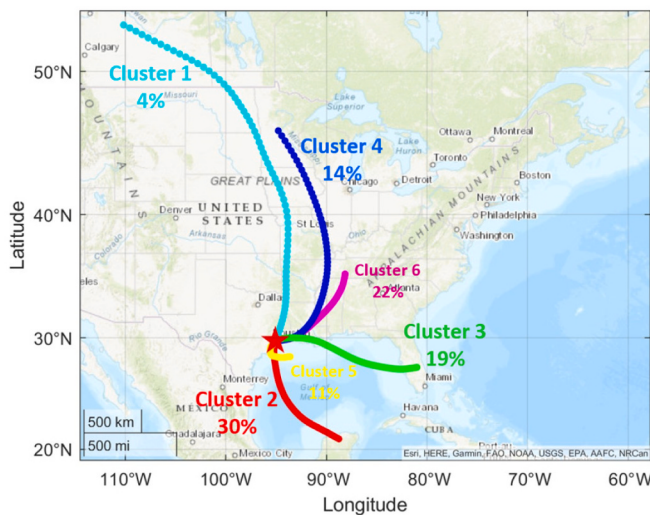


Fig. 2. Long-range transport pathway of air masses to the Houston region for receptors at (a) 2000 m and (b) 200 m AGL in Lynchburg Ferry. The left column represents the HYSPLIT-resolved trajectory clusters, and the right column shows variations in the transport pathways of hourly-released air parcels during September 2021. The colors in the right column correspond to the respective clusters indicated in the left column.

toluene being overestimated by approximately 0.49 ppb, while levels of benzene, ethane, and propane were underestimated by 0.37 ppb, 4.95 ppbv, and 3.39 ppbv, respectively. These observed biases can be attributed to uncertainties in emission inventories, the estimation of primary radicals' concentrations, and the modeling of PBL height dynamics, which are common challenges in photochemical models (Pan et al., 2015). Similar biases have also been noted in earlier studies conducted in the Houston area (Byun et al., 2007; Kim et al., 2011; Li et al., 2007). For example, Pan et al. (2015) modeled VOCs and ozone levels in southeast Texas during September 2013. Their findings indicated over-prediction of benzene, ethylene, toluene, and xylene, while isoprene and ethane were under-predicted. The biases between the simulated and observed VOCs were relatively substantial, reaching up to 200 %. Therefore, it is concluded that the biases between model estimations and observations in our study fall within an acceptable range for photochemical modeling and are consistent with earlier studies in the Houston area.

The evaluation of model performance during afternoon hours (12 PM – 3 PM) revealed that the model captured most of the variation ($R = 0.80$) in ozone but overestimated its levels by 6.41 ppbv (~15 %). This suggests a relatively improved performance of the model in predicting ozone levels during afternoon hours compared to a 24-h period (MB: 8.94 ppb, NMB: 33 %). The model exhibited a better representation of surface temperature with a slight underestimation of -0.06°C . For wind speed, the model captured 54 % of the variability but tended to overestimate it by 0.86 m/s (~32 %). In terms of ozone precursors, the model captured 36 % of the variability in NO_x levels with a negligible bias (~0.01 ppbv). As for the VOCs, the model captured up to ~25 % of the variability in the selected VOCs. Specifically, levels of benzene, ethane, and propane were underestimated by 62 % – 66 %, while the prediction for toluene showed almost no bias. Altogether, the model demonstrated reduced bias during afternoon hours, indicating a relatively improved performance during this specific period of the day.

3.2. Transport pathway of air masses

The regional-scale transport pathway of air masses is analyzed first, using the Lynchburg Ferry as an example, with similar patterns found at other locations (Fig. S4). Fig. 2 shows the main transport pathways of air masses arriving at the Lynchburg Ferry station at (a) 2000 m and (b) 200 m AGL during September 2021. The pathways were derived by applying the HYSPLIT cluster algorithm to all the 72-hour backward trajectories generated in hourly intervals. The backward trajectories with the receptor at 2000 m distinctly indicated four key source regions of air masses: (1) northern US, (2) south of the Gulf of Mexico, (3) east of the Gulf of Mexico, and (4) central US. The transported air parcels were dominantly from the central US (38 %) and south of the Gulf of Mexico (34 %), followed by the northern US (19 %), and east of the Gulf of Mexico (9 %). The backward trajectories with the receptor at 200 m were similar to those at 2000 m except for two additional clusters (cluster 5 and cluster 6). Cluster 5 represents the air parcels originating from the Gulf of Mexico, similar to cluster 2, but the source location is closer to the coastline than cluster 2. Air parcels from this cluster have remained closer to the investigated area for the duration of the analysis (i.e., 72 h). Cluster 6 is similar to cluster 4, both originating from the central US, but with slight differences in their directions. The trajectory analysis (right panels of Fig. 2) revealed that the ozone episodes were predominantly associated with the transport of pollutants from central and northern US (clusters 1, 4, and 6), while the source region of air masses during the non-episode days was mainly from the Gulf of Mexico (clusters 2, 3, and 5). This observation is in agreement with earlier studies reporting that ozone pollution events during late summer and early fall are typically associated with the synoptic circulation of northerly and easterly winds. The continental flow brings additional ozone and ozone precursors to the Houston area (which is already impacted by local emission sources), intensifying ozone production and

increasing its levels (Liu et al., 2015; Loughner et al., 2014; Mazzuca et al., 2017; Morris et al., 2006).

The HYSPLIT-modeled local transport pathway of air masses arriving at 200 m and 2000 m AGL in Lynchburg Ferry (Fig. S5) suggested that northerly air masses on September 6th – September 7th gradually deflected toward the eastern regions until September 11th. Recirculation of air masses was seen at the near-surface level (i.e., backward trajectories initialized at 200 m AGL) and occurred from September 8th – September 9th. The backward trajectory analyses for September 23rd – September 26th showed that air masses arriving at Lynchburg Ferry (both at 200 m and 2000 m AGL) were from northeast Houston on September 23rd while they gradually deflected toward eastern Texas and finally the Gulf of Mexico on September 26th. Unlike Episode 1, recirculation was not observed in the local transport pathway of air masses during Episode 2.

Fig. 3 shows the FLEXPART-modeled retroplume (backward in time) for dispersion of air masses released during 12 PM – 3 PM from the Lynchburg Ferry receptor at surface level (5 m – 15 m AGL), with similar dispersion patterns observed at other locations (Fig. S6). FLEXPART output for September 6th is consistent with HYSPLIT for the same period in that both models predicted air masses started rotating clockwise from the Gulf of Mexico toward northern regions. Starting from September 7th, the transport pathways have further deflected to the northeast directions, and finally, they changed toward eastern Texas from September 10th – September 11th. The vertical profile of retroplume showed that the plume experienced subsidence from higher altitudes (1000 m – 2000 m) during Episode 1. By overlapping the transport pathway of air masses with the modeled ozone levels using the method described in Section 2.2.4, we found elevated ozone levels within the range of 55 ppbv – 65 ppbv on September 7th and September 9th, coinciding with the transport pathway passing through 1000 m – 2000 m AGL altitude. This shows the vertical transport of air masses potentially brought ozone from higher altitudes to the surface level during Episode 1 (Fig. S7). The FLEXPART-modeled retroplume shows an accumulation of polluted air parcels across the Houston region during September 8th – September 9th. This observation agrees with HYSPLIT trajectories depicting recirculation of air masses across the Houston area in Episode 1. Recirculation and the accumulation of pollutants over the Houston area usually occur during pollution episodes when a sea breeze develops after synoptic winds transport pollutants to the area. In such cases, the northerly synoptic flow that transports air masses from land to sea interacts with the sea breeze, leading to stagnant conditions (Darby, 2005; Loughner et al., 2014; Mazzuca et al., 2017; Morris et al., 2010).

During Episode 2, the source region of air masses was northern Texas on September 23rd, and it switched toward eastern regions from September 24th to September 26th. Unlike Episode 1, the major source region of air masses remained at altitudes <1000 m for the duration of analysis, precluding the potential impact of ozone from higher altitudes on the surface-level ozone during Episode 2.

3.3. Ozone production tendency

As revealed from the transport analysis above, different air masses that impacted the Houston region would have distinct chemical characteristics and, thus, different ozone formation mechanisms. To investigate such chemical differences, we showed in Fig. 4 the CAMx-predicted ozone production rate (PO_3) during ozone peak hours (12 PM – 3 PM) separated between non-episode and episode days and the breakdown of PO_3 between VOC-limited (VOC-limited PO_3) and NO_x -limited ($\text{NO}_x\text{-limited PO}_3$) regimes. CAMx follows the approach suggested by Sillman (1995) to classify ozone formation tendency based on the ratio between hydrogen peroxide (H_2O_2) and nitric acid (HNO_3) production rates (shown in Fig. S9) in which $\text{P}(\text{H}_2\text{O}_2)/\text{P}(\text{HNO}_3) > 0.35$ is indicative of a NO_x -limited regime, and < 0.35 is indicative of a VOC-limited regime. This metric represents the ratio of two instantaneous production rates and can be applied to spatially and temporally evolving

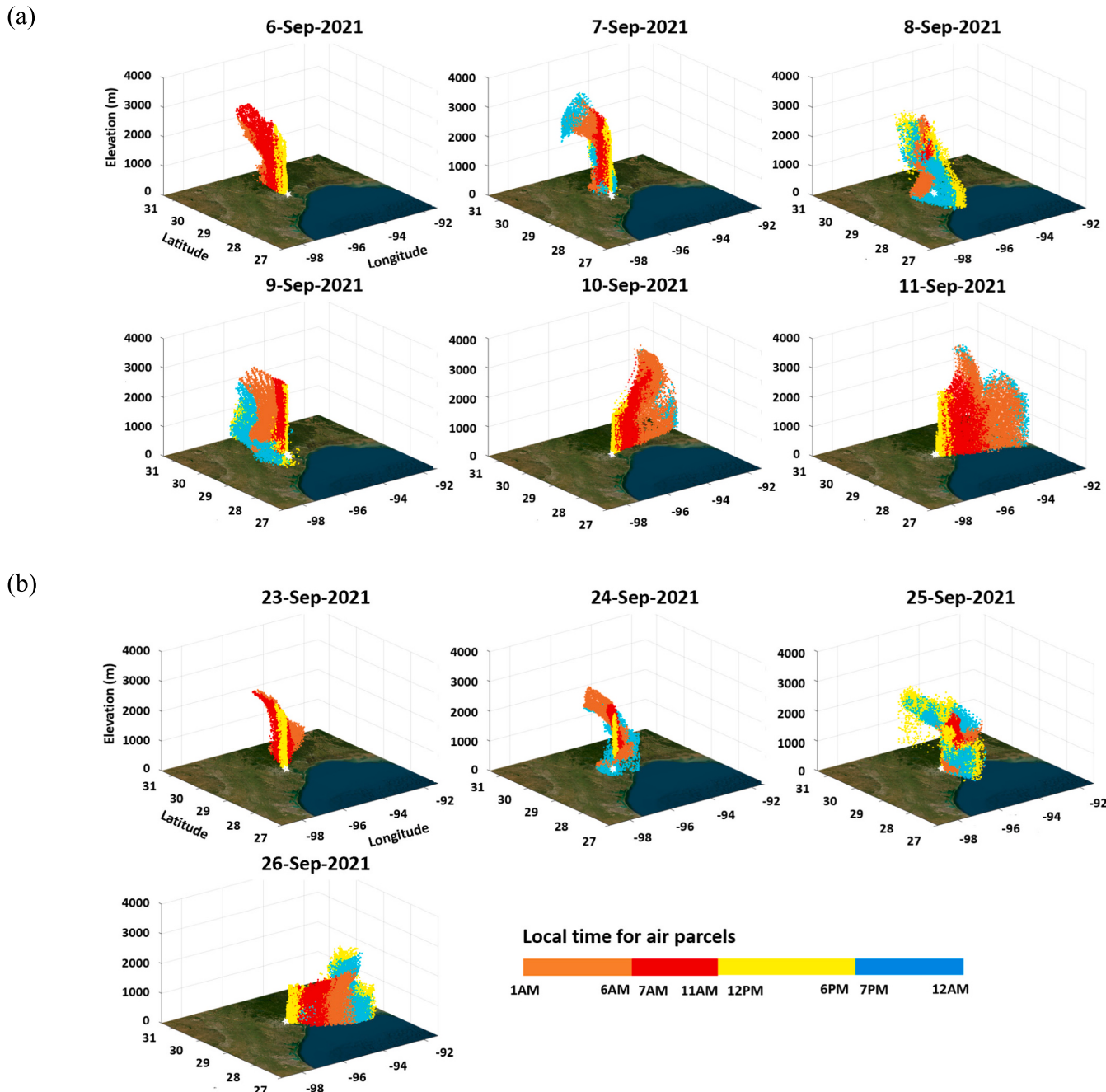


Fig. 3. Results of FLEXPART-WRF backward trajectory analysis with the receptor at 15 m AGL in Lynchburg Ferry during (a) Episode 1 and (b) Episode 2. The colored dots indicate the time (CST) of air masses along the trajectory pathway. The location of the Lynchburg Ferry site is shown by a white asterisk.

air masses (Vermeuel et al., 2019). According to Fig. 4(a), non-episode days saw a net chemical loss of ozone over the region ($\text{PO}_3: -0.11 \pm 6.90 \text{ ppb/h}$). However, the ozone production rate surged to $1.70 \pm 6.21 \text{ ppb/h}$ and $1.50 \pm 6.02 \text{ ppb/h}$ during Episodes 1 and 2, respectively, across the study domain (d03). The modeled PO_3 hotspots were predominantly located across Houston, the HSC, and Galveston Bay. Earlier field campaigns in the Houston area (i.e., TexAQS, TexAQS II, and DISCOVER-AQ) have also observed the greatest ozone production rates over Houston and the HSC, which are impacted by high emissions of ozone precursors (Mazzuca et al., 2016; Zhou et al., 2014). Our modeled PO_3 ranged from 4 ppb/h to 8 ppb/h for the urban districts across the HGB region, with hotspots (12 ppb/h and higher) observed near Galveston Bay and the HSC. Although PO_3 was not directly measured during the TRACER-AQ campaign, our CAMx-modeled PO_3 was within the

range of reported values from earlier studies in the region reporting $\text{PO}_3 > 10 \text{ ppb/h}$ in locations with high NO_x and VOC emissions, while it could be below 10 ppb/h farther away from the urban areas with lower ozone precursor emissions (Berkowitz et al., 2004; Lei et al., 2004; Mazzuca et al., 2016; Ying and Krishnan, 2010).

Fig. 4(b) shows mean VOC-limited PO_3 during 12 PM – 3 PM within non-episode and episode days. During non-episode days, the spatial distribution of VOC-limited PO_3 encompassed the urban areas of Houston, the HSC, and Galveston Bay. During ozone episodes, however, VOC-limited PO_3 hotspots were confined to the industrialized areas of the HSC and eastern Houston. According to Fig. 4(c), a NO_x -limited regime was predicted across urban/suburban districts of the Houston metropolitan area, and NO_x -limited PO_3 increased by $\sim 140\%$ and $\sim 105\%$ during Episodes 1 and 2 (compared with non-episode days),

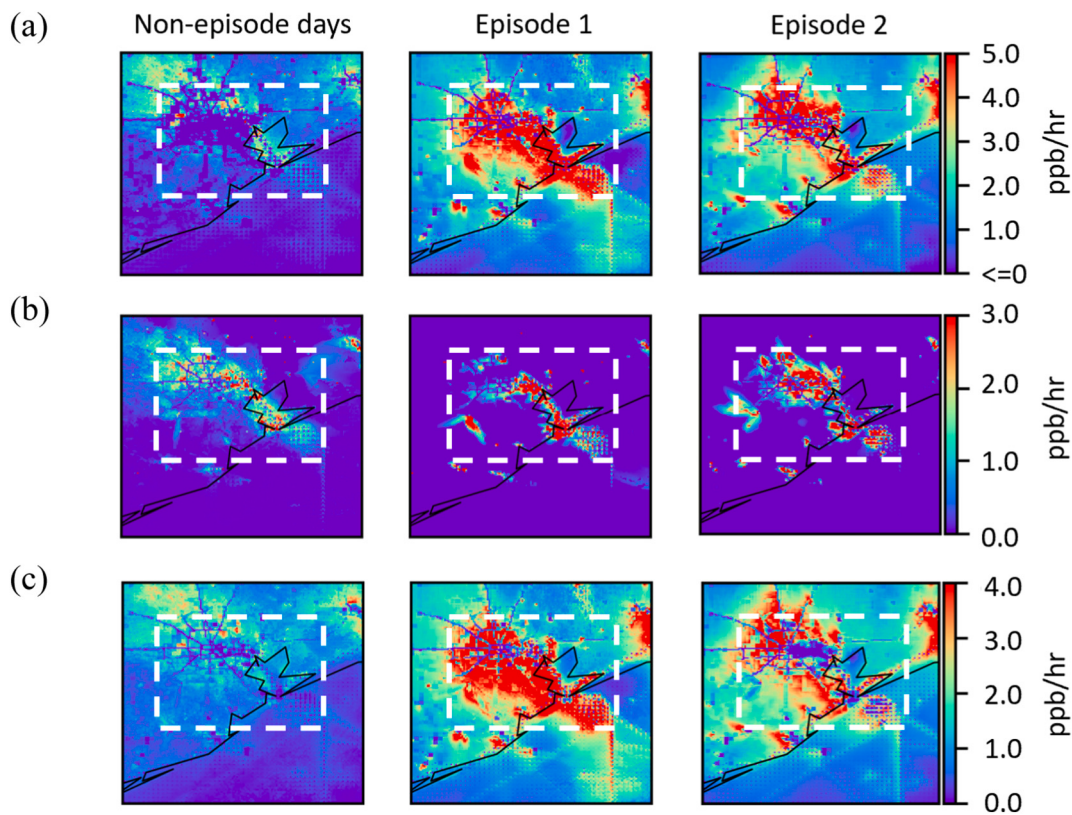


Fig. 4. Spatial variations in CAMx-resolved (a) net ozone production rate, (b) VOC-limited ozone production rate, and (c) NO_x-limited ozone production rate averaged during 12 PM – 3 PM for non-episode and episode days. The corresponding mean \pm SD values for each parameter across d03 and the white dashed domain (i.e., Southeast Houston, HSC, and Galveston Bay) are summarized in Table 1. (Episode 1: Sep. 6th – Sep. 11th, Episode 2: Sep. 23rd – Sep. 26th, non-episode: Sep. 1st – Sep. 5th + Sep. 12th – Sep. 16th + Sep. 20th – Sep. 22nd + Sep. 27th – Sep. 30th).

respectively, across the study domain (d03). Altogether, we conclude that both VOC-limited and NO_x-limited ozone formation mechanisms have contributed to the increased ozone production rates over the Houston area. The enhanced ozone production might be associated with variations in ozone formation tendency as well as the transport of ozone precursors. Ozone production is generally NO_x-sensitive during noon/afternoon (Chen and Brune, 2012; Ren et al., 2013); thus, VOC-limited PO₃ from 12 PM – 3 PM may not efficiently capture the variations in VOC-sensitive ozone formation during the TRACER-AQ campaign. Our analysis of the 24-h mean ozone production rate also revealed that VOC-limited PO₃ across Houston, the HSC, and Galveston Bay increased by ~80 % and ~110 % during Episode 1 and Episode 2, respectively (Fig. S8). Similarly, 24-h mean NO_x-limited PO₃ experienced a 2-fold increase during ozone episodes across the investigated domain (d03). Therefore, the elevated ozone production rates were not limited to ozone peak hours (i.e., 12 PM – 3 PM), rather CAMx predicted increased 24-h mean VOC-limited PO₃ and NO_x-limited PO₃ during ozone episodes.

To further investigate spatial variations in ozone formation sensitivity and compare it with hotspots of CAMx-derived VOC-limited and NO_x-limited ozone productions, the ozone production dependence on NO_x and VOCs is evaluated based on the ratio of radical loss (L_N) through reaction with NO_x to the total primary radical production (Q) (Kleinman, 2005; Kleinman et al., 2001). In this method, an L_N/Q of 0.5 is defined as the threshold to differentiate VOC sensitivity (L_N/Q > 0.5) from NO_x sensitivity (L_N/Q < 0.5). The L_N/Q calculation is particularly suitable for analyzing urban plumes where air parcels typically transition from high NO_x near emission sources to low NO_x at some distance away (Vermeuel et al., 2019), as can be observed in the Houston-Galveston-Brazoria region with numerous emission sources concentrated in the HSC. Fig. 5 shows afternoon ozone production tendency

based on L_N/Q during non-episode and episode days. The Houston metropolitan area was primarily in a VOC-limited regime during non-episode days. This observation is in agreement with previous studies identifying urban Houston as dominantly VOC-sensitive in terms of ozone production tendency (Mazzuca et al., 2016; Zhou et al., 2014). However, as shown in Fig. 5, Houston moved toward more NO_x sensitivity during ozone episodes so that the VOC-limited regions were restricted to downtown Houston and the HSC (these regions remained VOC-limited even during ozone episodes). Similarly, analysis of 24-hour mean L_N/Q revealed that ozone production tendency switched from VOC-limited to NO_x-limited regime (except for downtown Houston and the HSC) during ozone episodes (Fig. S9). The observed transition in ozone production tendency from VOC-sensitive to NO_x-sensitive conditions during ozone episodes is likely due to the potential variations in the atmospheric levels of ozone precursors (i.e., NO_x or VOCs) across the Houston area (Kleinman et al., 2005), which will be analyzed in Section 3.5.

3.4. Contribution of different processes in ozone formation

To characterize the impacts of different chemical and physical processes on the elevated ozone formation, we analyzed the contribution of chemistry, transport (advection and diffusion), and deposition. Fig. 6 shows the contribution of different atmospheric processes to ozone formation across the study domain (i.e., d03). According to Fig. 6(a), transport is the dominant process that influences ozone levels in the region. This finding aligns with previous studies reporting that a substantial portion of ozone in the Houston-Galveston-Brazoria region is transported from outside of the region during specific synoptic-scale circulations (Langford et al., 2009). In accordance with expectations and as shown in Fig. 6(b), the role of chemistry in ozone production

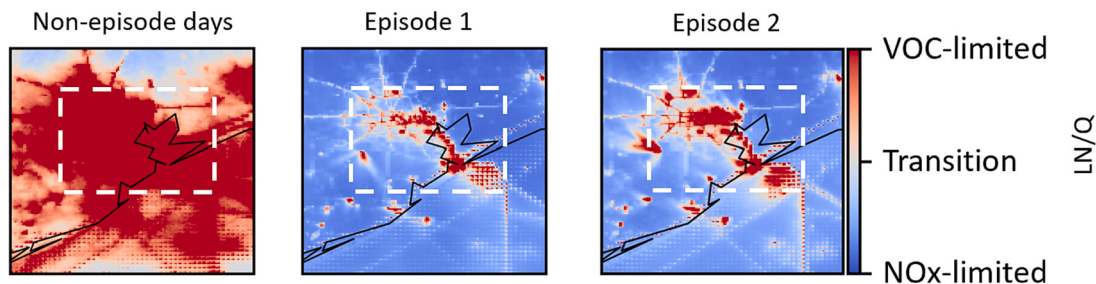


Fig. 5. Ozone production sensitivity based on CAMx-resolved L_N/Q during 12 PM – 3 PM in non-episode and episode days.

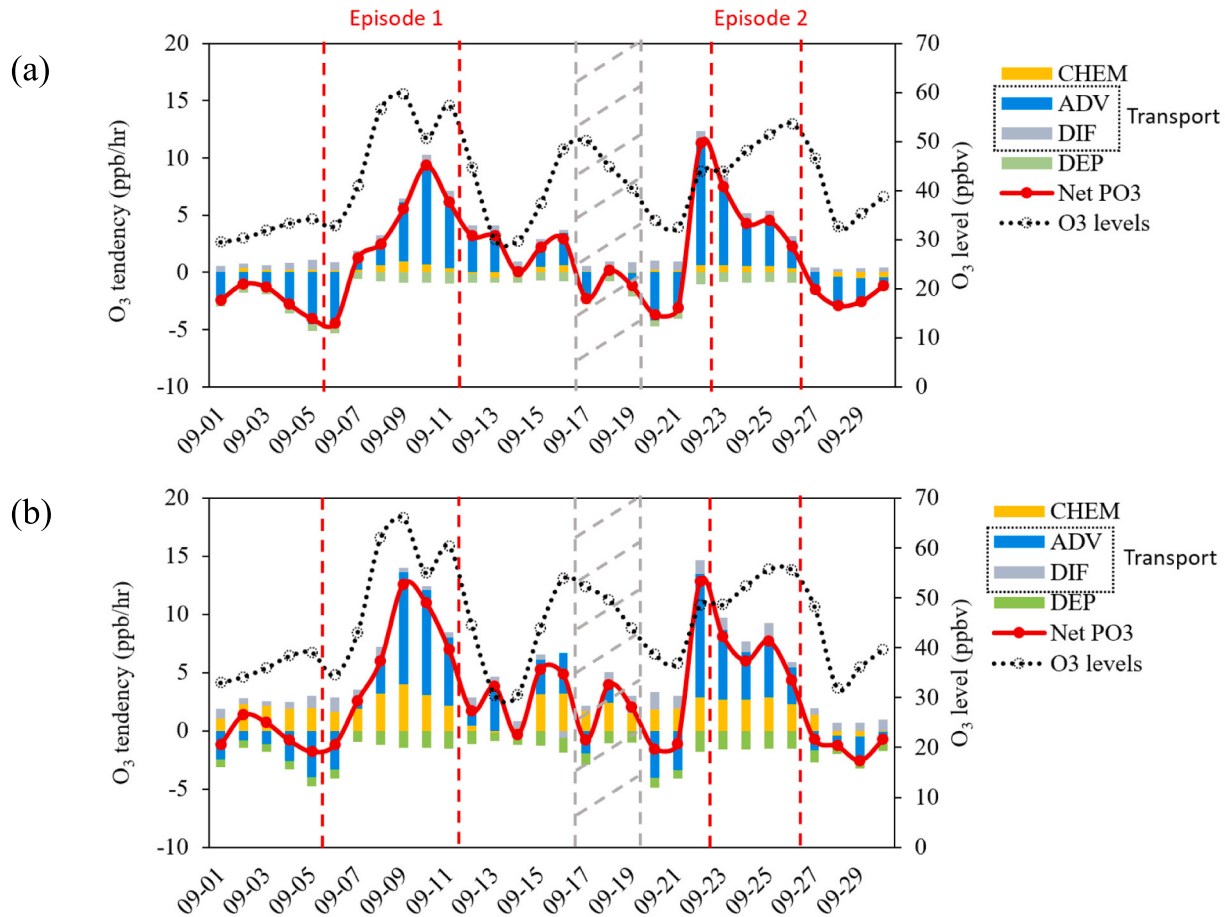


Fig. 6. Contributions of chemical processes (CHEM), advection (ADV), diffusion (DIF), and deposition (DEP) to ozone formation during September 2021, represented by (a) 24-h mean values, and (b) midday hours mean (12 PM – 3 PM).

becomes prominent during the midday hours (12 PM – 3 PM). Within early September, chemistry exhibited a significant contribution to ozone production (~ 1.43 ppb/h) whereas advection (~ -2.19 ppb/h) played a compensating role, resulting in a net condition of ozone destruction. This balance shifted in Episode 1, wherein both chemistry and transport contributed more significantly to ozone production, with rates of approximately 2.66 ppb/h and 4.16 ppb/h, respectively. Similarly, chemistry (~ 2.62 ppb/h) and transport (~ 4.60 ppb/h) emerged as the primary drivers to ozone formation in Episode 2. The process analysis results suggested that the transport of ozone was the major contributor to ozone formation during ozone episodes followed by the chemical production of ozone from precursors.

3.5. Variations in ozone precursors

In this section, we investigate the variations in the levels of NO_x and speciated VOCs during ozone episodes to identify the major drivers of the transition from VOC-limited to NO_x-limited conditions across the Houston area presented above. We compare ozone precursors between non-episode and episode days for 24-hour and afternoon mean levels of NO_x and VOCs. Evidence is also provided to show how variations in ozone precursors have led to enhanced ozone production rates during episode days.

Fig. 7 shows the modeled levels of NO_x and peroxyacetyl nitrate (PAN) from 12 PM – 3 PM across the Houston area. The afternoon levels of NO_x decreased by $\sim 40\%$ during ozone episodes (**Fig. 7(a)**). However, 24-hour NO_x levels increased by approximately 10 % (in Episode 1) and 25 % (in Episode 2) across the Houston area and the HSC (Fig. S10(a)).

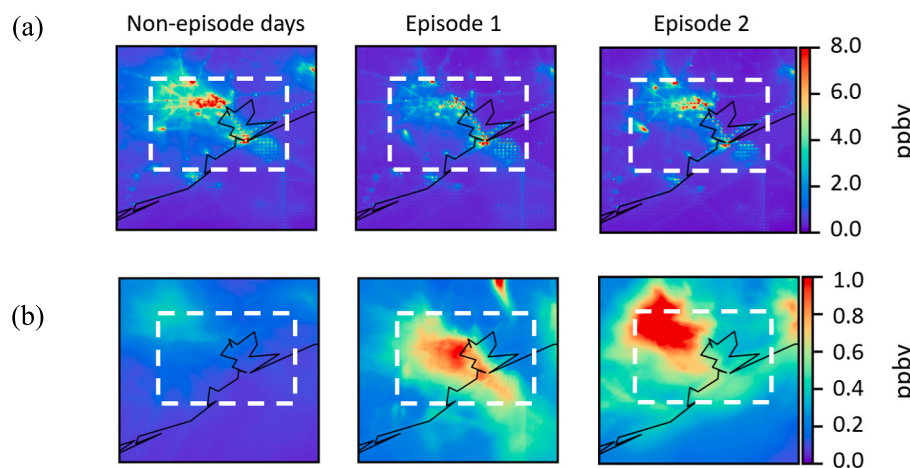


Fig. 7. Spatial variations in levels of (a) NO_x , and (b) PAN during non-episode and episode days. All the parameters were averaged during 12 PM – 3 PM local time. The corresponding mean \pm SD values for each parameter across d03 and the white dashed domain (i.e., Southeast Houston, HSC, and Galveston Bay) are summarized in Table 1.

Analysis of measured NO_x levels among the selected sites revealed that the 24-hour mean NO_x increased by 35 % – 70 % and 35 % – 150 % during Episode 1 and Episode 2, respectively (Fig. S11). TAMIS observations showed that NO_x levels experienced, on average, ~25 % (in Episode 1) and ~35 % (in Episode 2) reduction during 12 PM – 3 PM across the selected sites, thus validating the results of the CAMx model. The afternoon reduction in NO_x levels across the study domain during ozone episodes (compared with non-episode days) can be explained by the photochemical removal of NO_x when ozone production peaks (Berezina et al., 2020; Kleinman et al., 2005). In contrast, the enhanced 24-hour NO_x level during ozone episodes is partly associated with stagnation and accumulation of pollutants (according to Section 3.2) since regions with elevated NO_x levels were limited to local emission hotspots such as major highways in Houston and the HSC (rather than the entire model domain). Furthermore, NO_x cannot survive transport over long distances due to its relatively short lifetime (Brown et al., 2013; Goldberg et al., 2020). However, NO_x may have been transported to the region by means of PAN, a well-known tropospheric reservoir of NO_x that can transport over long distances. PAN is mainly produced from the oxidation of VOCs in the presence of NO_x (as well as proxy radicals (HO_x)) and is removed by thermal decomposition in the lower troposphere (Fischer et al., 2014; Grosjean et al., 1994; Zhang et al., 2021). Fig. 7(b) shows the spatial distribution of PAN across the study area in the afternoon. While PAN levels increased by a factor of ~3 during the ozone episodes, the hotspots of PAN were found within Houston, and the levels of this pollutant decreased away from urban areas. Similar features were found for the 24-hour mean PAN levels across the Houston region (Fig. S10(b)). Therefore, enhanced levels of PAN in Houston during ozone episodes were mostly due to the local formation of PAN, which suggests that NO_x had not been transported to the region by means of PAN. Altogether, we infer that increased daily levels of NO_x during ozone episodes are associated with meteorological conditions that trap locally emitted NO_x and lead to the accumulation of pollutants near the source regions. Thus, variations in NO_x levels limited to major highways and industrialized districts cannot be solely responsible for the observed transition to NO_x -limited conditions over the rest of the Houston metropolitan area, suggesting the potential impact of elevated VOCs on changing the ozone formation tendency.

Fig. 8 shows the modeled surface concentrations of VOCs classified by different functional groups during non-episode and episode days. VOCs generally contribute to ozone formation by reacting with OH radicals, leading to the formation of proxy radicals (e.g., HO_2) which later participate in NO to NO_2 conversion and ozone formation. According to Fig. 8, paraffins increased by ~120 % (Episode 1) and 45 %

(Episode 2) across the investigated domain (d03). The levels of olefins and aromatics remained almost comparable between non-episode and episode days. Concentrations of biogenic VOCs (BVOCs, consisting of isoprene and monoterpenes) decreased by ~40 % and ~60 % during Episode 1 and Episode 2, respectively. This decrease reflects enhanced oxidation of BVOCs during ozone episodes (as opposed to lower emissions) as BVOCs emissions were approximately the same (differences smaller than 15 %) between non-episode and episode days. CAMx modeled a remarkable increase of aldehydes (consisting of formaldehyde, acetaldehyde, propionaldehyde, and higher aldehydes) by approximately 95 % in Episode 1 (and correspondingly 30 % in Episode 2). Lastly, levels of ketones (consisting of acetone and compounds with a ketone carbon bond) surged by a factor of 2.5 and 1.5 in Episodes 1 and 2, respectively. Similar results were found for the 24-hour mean levels of mentioned functional groups during non-episode and episode days (Fig. S12). Olefins and aromatics (mainly emitted from petrochemical and industrial sectors) are highly reactive VOCs with relatively short lifetimes and thus cannot be efficiently transported across long distances (Ma et al., 2021; Xue et al., 2014). Similarly, BVOCs are too short-lived to survive transport (Brown et al., 2013). On the other hand, paraffins have low reactivity and long lifetimes and thus can be transported in the atmosphere over long distances and are representative of aged emissions (De Gouw et al., 2005; Xie and Berkowitz, 2006). Furthermore, aldehydes (e.g., formaldehyde) are produced by the oxidation of VOCs and act as temporary reservoirs releasing HO_x free radicals. Formaldehyde participates in catalytic cycles producing ozone and has a relatively long lifetime (Alvarado et al., 2020). Oxygenated VOCs such as acetone can also be present in aged air masses (Zhang et al., 2004). Analyzing the temporal variations in levels of speciated VOCs revealed that enhanced VOCs during ozone episodes were mainly driven by functional groups with longer lifetimes, such as paraffins and aged VOCs, suggesting the transport of long-lived species to the Houston region. It has been documented that paraffins originate from various sources, such natural gas, fuel combustion/evaporation, and industrial sectors (Buzcu and Fraser, 2006; Jorquera and Rappenglück, 2004; Lechner and Rappenglück, 2010). Aldehydes and ketones (known as carbonyls) are mainly emitted from petrochemical plants, waste treatment facilities, traffic (resulting from incomplete combustion of hydrocarbons), and industrial machinery/processes (H. K. Wang et al., 2010; Zhao et al., 2022). Additionally, biogenic sources and oxidation products of biogenic VOCs contribute to the levels of carbonyls (Chen et al., 2014). Based on the transport pathway of air masses modeled by trajectory analysis (Section 3.2), these VOCs have likely originated from eastern Texas and Louisiana before arriving in Houston. Specifically, the Beaumont–Port–Arthur

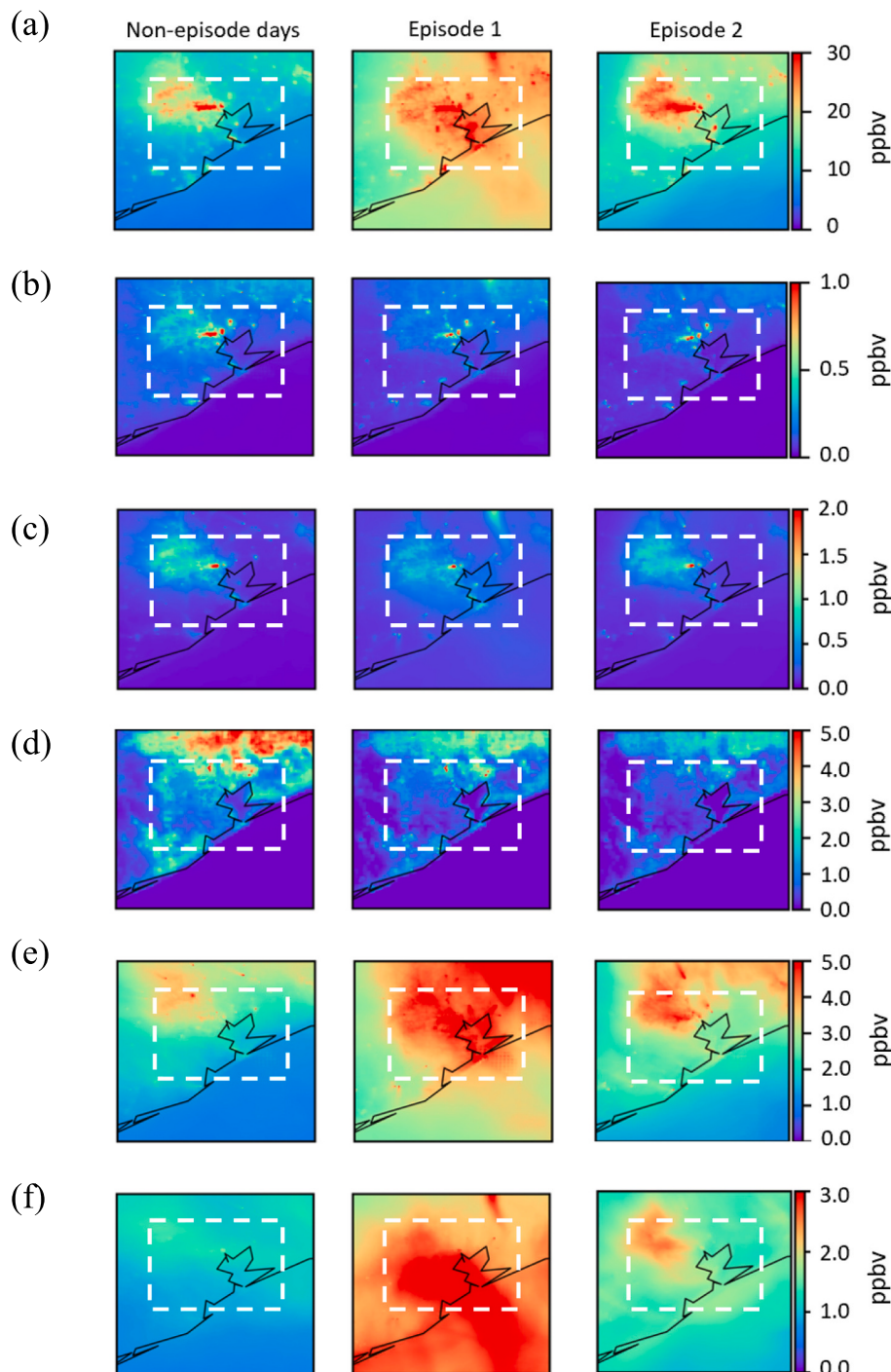


Fig. 8. CAMx-simulated surface levels of (a) paraffins, (b) olefins, (c) aromatics, (d) biogenic VOCs, (e) aldehydes, and (f) ketones during 12 PM – 3 PM within non-episode and episode days. The corresponding mean \pm SD values for each parameter across d03 and the white dashed domain (i.e., Southeast Houston, HSC, and Galveston Bay) are summarized in Table 1.

(BPA) area is a host of several industrial and petrochemical chemical plants emitting significant amounts of VOCs to the atmosphere and can influence the Houston area under easterly winds (Ge et al., 2021a). Furthermore, the heavily forested regions in eastern Texas and Louisiana serve as sources of biogenic VOCs, which can form aldehydes and ketones through photochemical reactions (Zhang et al., 2017). The contributions of photochemistry, transport, and local emissions to the elevated levels of paraffins, aldehydes, and ketones are shown in Fig. S13. Based on the results of IPR analysis, advection accounted for on

average 36 % of variations in paraffins, while its impact was relatively minimal compared to local emissions during non-episode days. Photochemistry had minimal influence on paraffin levels, as paraffins have low reactivity and do not significantly participate in photochemical reactions (De Gouw et al., 2005; Xie and Berkowitz, 2006). During ozone episodes, local photochemistry played a major role in the formation of aldehydes and ketones by contributing to 50 % and 42 % of their variations, respectively. Similarly, transport processes accounted for 34 % and 44 % of the variations in the levels of aldehydes and ketones, while

local emissions had a minimal influence (13 % – 16 %).

While the Houston area was impacted by higher-than-usual levels of VOCs during ozone episodes, NO_x levels remained almost the same away from major emission sources, resulting in excessive ambient VOCs concentrations and NO_x-limited conditions. The elevated levels of NO_x (mainly due to stagnation and the accumulation of pollutants) over industrial districts, particularly near the HSC, counterbalanced the effects of the transported VOCs, and those areas remained VOC-limited.

The impact of transported VOCs on ozone chemistry was investigated based on OH radical loss rate through reaction with VOCs. This parameter is a robust metric to estimate the role of VOCs in ozone formation quantitatively (Goldan et al., 2004; Li et al., 2015). Atmospheric radicals such as OH initiate VOC oxidation and produce hydroperoxy (HO₂) and organic peroxy radicals (RO₂), leading to ozone formation in the presence of NO_x (Heard and Pilling, 2003; Lew et al., 2020). Fig. 9 shows the variations in afternoon OH loss and HO₂ production rates during non-episode and episode days. According to the figure, the OH loss rate through reaction with VOCs increased by ~100 % and ~45 % during Episodes 1 and 2, respectively. During ozone episodes, OH levels increased by ~55 % due to higher OH production rates, particularly across Houston and the HSC (Fig. S14). As shown in Fig. S14, the enhanced levels of OH were associated with higher photolysis of ozone (and to some extent VOCs, and nitrous acid (HONO)) that have been identified as major processes leading to OH formation in the region (Vizuete et al., 2008; Zhou et al., 2014). Therefore, the increase in OH loss rate through reaction with VOCs is explained by the elevated levels of VOCs (as shown in Fig. 8) and OH across the Houston area. As a result, the HO₂ production rate increased by ~130 % (Episode 1) and ~70 % (Episode 2) compared with non-episode days, making a favorable environment for ozone formation. Similar trends were also observed for the 24-hour mean OH loss and HO₂ production rates (Fig. S15). Lastly, the produced HO₂ participates in NO to NO₂ conversion, which ultimately leads to ozone formation (Kleinman et al., 2002; Lew et al., 2020). Based on the above discussion and due to the predominant role of NO_x availability in the ozone formation process, ozone production hotspots (as shown in Fig. 4) were primarily across the HSC, where higher levels of NO_x were observed (Fig. 7). This underscores the necessity of tailored emission control strategies that specifically target NO_x sources within the HSC area.

3.6. Transport and formation of ozone along the retroplume

As discussed in Section 2.2.4, overlapping CAMx chemical fields with

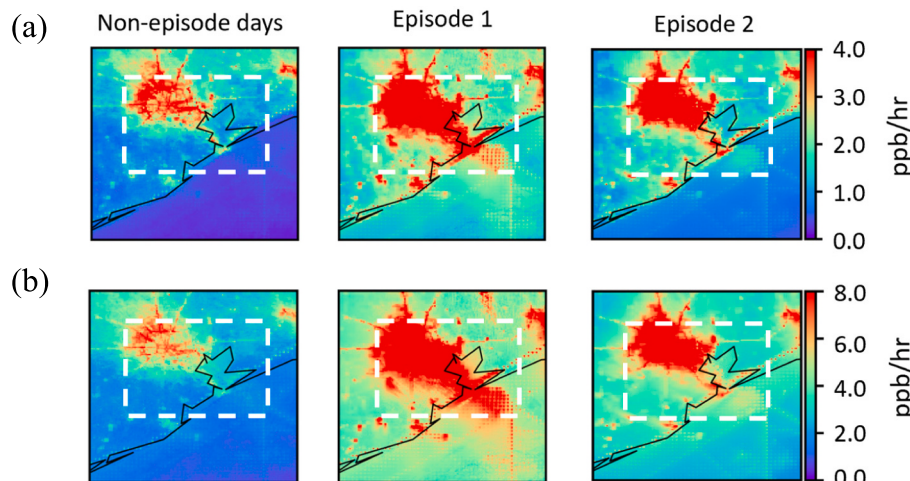


Fig. 9. Spatial variations in (a) OH loss rates by reaction with VOCs and (b) HO₂ production rates during 12 PM – 3 PM in non-episode and episode days. The corresponding mean ± SD values for each parameter across d03 and the white dashed domain (i.e., Southeast Houston, HSC, and Galveston Bay) are summarized in Table 1.

FLEXPART backward simulations provides details on the physico-chemical processes that occurred throughout the retroplume. Fig. 10 shows the time series of folded FLEXPART-CAMx retroplume averaged throughout the transport pathway for daily releases. According to Fig. 10(a), ozone in the retroplume increased from ~47.3 ppbv on September 5th to 57.0 ± 4.6 ppbv during September 6th – September 11th, while it dropped to ~32 ppbv on September 13th, suggesting elevated levels of ozone in the transported plume during Episode 1. Furthermore, the ozone levels peaked on September 8th (with an average level of ~62 ppbv along the retroplume), likely due to the recirculation of air masses over the Houston area (shown in Fig. 3) and ozone hotspots. The formation of ozone during transport in Episode 1 was dominantly NO_x-limited (0.84 ± 0.34 ppb/h) compared with being VOC-limited (0.18 ± 0.13 ppb/h). The contribution of VOCs to ozone formation decreased from ~39 % on September 4th – September 5th to 17 % during Episode 1, which shows the dominant role of NO_x-limited ozone production during the transport pathway. Fig. 10(b) shows that the mean levels of NO_x and PAN increased slightly during September 6th – September 9th (compared with pre-Episode 1). However, the elevated levels of these species were observed when the plume was only 2–3 h away from the receptor (Fig. S16), indicating the impact of NO_x emissions from local industries. According to Fig. 10(c), the levels of VOCs in the plume increased by 2–4 times during Episode 1, which is in line with Section 3.4 on the importance of the transport of VOCs to the region. More specifically, the levels of aldehydes, paraffins, and ketones remained almost constant along the plume, while those of short-lived reactive VOCs, such as olefins, aromatics, and BVOCs were more variable given their photochemical evolution (Fig. S16).

In Episode 2, a state of net ozone destruction on September 21st switched to net ozone production within September 23rd – 26th, during which ozone levels along the retroplume increased from ~37 ppbv (pre-Episode 2) to 49.9 ± 7.3 ppbv (during Episode 2). In contrast to Episode 1, ozone formation along the retroplume during Episode 2 was a combination of VOC-limited (0.68 ± 0.71 ppb/h) and NO_x-limited (0.57 ± 0.21 ppb/h) ozone productions. Analysis of ozone precursors showed NO_x and PAN increased by a factor of ~2 and ~4, respectively, during Episode 2 (compared with pre- and post-Episode 2). The elevated levels of NO_x and PAN were observed within 2–4 h before the plume arrived at Lynchburg Ferry (except for September 25th), showing the prominent role of local emissions. According to Fig. S16, the plume contained high levels of NO_x (i.e., 2.67 ± 0.55 ppbv) for almost 10 h before arriving at Lynchburg Ferry on September 25th, which is likely caused by the stagnant conditions where air masses remained close to the receptor and

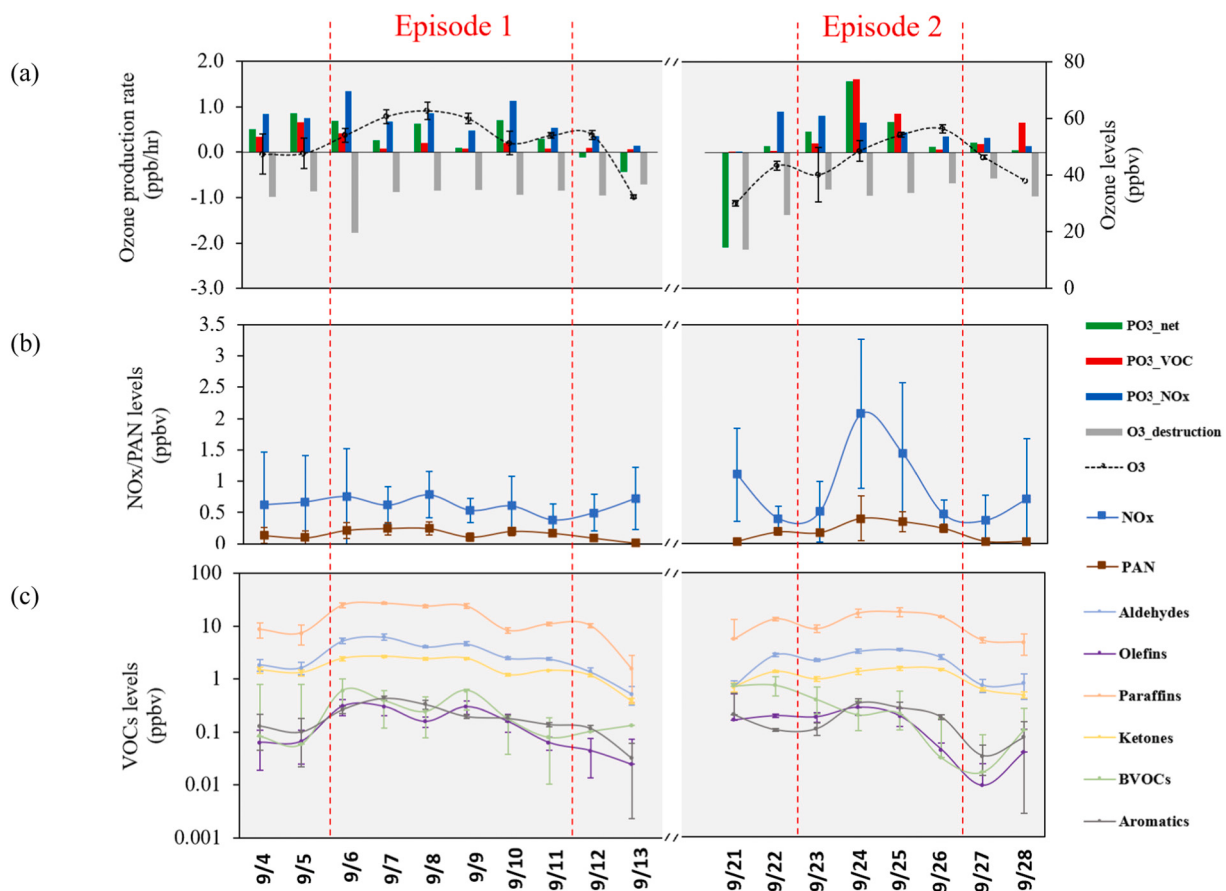


Fig. 10. Plume evolution based on variations in mean (a) ozone/ozone production, (b) NO_x/PAN, and (c) volatile organic compounds throughout the FLEXPART-modeled retroplume. Error bars correspond to one standard deviation. The analysis encompasses two days prior to ozone episodes onset (i.e., Sep. 4th – 5th and Sep. 21st – 22nd) and two days after the termination of ozone episodes (i.e., Sep. 12th – 13th and Sep. 27th – 28th).

the Houston area (shown in Fig. 3). This also led to the accumulation of PAN in the retroplume as a result of the oxidation of NO_x to PAN. Similar to Episode 1, the levels of VOCs (except BVOCs) increased on average by a factor of ~2 during Episode 2. Therefore, due to the notable increase in NO_x levels along the retroplume, ozone formation tendency moved toward VOC sensitivity, resulting in VOC-limited ozone production. This analysis showed the photochemical aging of air masses and revealed the impact of ozone precursors along the transport pathway on ozone formation and accumulation.

3.7. Consideration of model uncertainties and result interpretation

Uncertainties in atmospheric modeling can arise from input data (such as meteorology and emissions), model parameterizations, and the formulation of physical and chemical processes in the atmosphere (Rao, 2005; Sharma et al., 2017; Srinivas et al., 2016). Modeling the atmospheric meteorology that governs the transport and mixing of ozone and its precursors may be challenging, particularly in regions characterized by complex local-scale circulations such as the Houston area (Pirovano et al., 2007). Furthermore, uncertainties exist in estimating emissions from different sources (Holnicki and Nahorski, 2015). In a case study, Dunker et al. (2020) evaluated the uncertainty in modeling ozone production using CAMx in Eastern Texas. The authors investigated sensitivity of ozone production to various parameters and concluded that the chemistry (i.e., parameters in a chemical mechanism, such as rate constants and stoichiometric coefficients) and emission estimation contributed to the largest uncertainties in modeling ozone formation, followed by dry deposition of ozone, and its boundary conditions. While the interactions between these parameters can introduce additional

uncertainty in the model, their impact is expected to be negligible (Beddoes et al., 2017; Dunker et al., 2020). Uncertainties in atmospheric trajectory analysis are associated with assumptions regarding random motions in the atmosphere (such as turbulence and convection mechanics) as well as the simulation of the wind field, mixed layer depth, temperature, and friction velocity (Srinivas et al., 2016; Zhang et al., 2014). Overlapping CAMx chemical fields with FLEXPART backward simulations can introduce an extra source of uncertainty due to inherent differences in numerical diffusion between Eulerian and Lagrangian models. To mitigate this discrepancy, Owen and Honrath (2009) and Zhang et al. (2014) suggested employing high-resolution simulations. Altogether, it is important to interpret the results with caution and note that the presented outcomes are based on model simulations that may not perfectly capture the true atmospheric conditions.

4. Summary and conclusions

In this study, we investigated ozone pollution episodes during the 2021 TRACER-AQ campaign in Houston, Texas. Hourly levels of surface ozone measured at selected TCEQ monitoring sites across the Houston metropolitan area surged by, on average, ~80 % during ozone episodes. This increase was more noticeable for Houston and the HSC. The non-episode days typically have air masses originating from the Gulf of Mexico, while ozone episode days (i.e., September 6th–September 11th, and September 23rd–September 26th) were associated with the transport of pollutants from central/northern US, revealing the impact of synoptic scale circulation patterns on ozone levels in Houston. The synoptic flows then interacted with local land-sea breeze, leading to stagnation and accumulation of ozone in the region. The ozone episodes

showed different transport patterns on a local scale. Episode 1 was impacted by recirculation and stagnation of air masses across the Houston area that trapped local emissions near sources and led to the accumulation of pollutants. Episode 2 was not influenced by the recirculation of air pollutants over the region. Transported air masses brought ozone precursors, especially VOCs, to the area. The surface levels of paraffins, aldehydes, and ketones increased by roughly 115 %, 95 %, and 160 %, respectively, during Episode 1. Similar observations were found for Episode 2. Unlike VOCs, NO_x levels have not experienced significant variations during ozone episodes, most likely due to the short lifetime of NO_x that cannot survive long-range transport. Therefore, elevated levels of VOCs (when NO_x remained almost the same across the region) have switched the ozone formation tendency from VOC-limited to NO_x-limited regime over the Houston metropolitan area. However, since the impact of local NO_x emissions from mobile sources and industrial sectors was most significant near downtown Houston and the HSC, these areas remained in VOC-limited conditions during the ozone episodes regardless of the transported VOCs to the region. As a result, the excessive VOCs switched a general ozone destruction condition (during non-episode days) over the Houston area to a net ozone production regime during ozone episodes. This transition was intensified over Houston and the HSC as the transported VOCs participated in ozone formation in VOC-limited conditions. Finally, our analysis revealed that the transported plumes during Episode 1 and Episode 2 had different characteristics in terms of ozone formation mechanisms. The plume evolution during Episode 1 showed that ozone formation was generally NO_x-sensitive across the transport pathway while both NO_x and VOCs contributed almost equally to ozone formation throughout the plume in Episode 2. The results of this study revealed the complex nature of ozone formation in the Houston area based on the interplay between precursor emissions, meteorological patterns, and atmospheric photochemistry. This comprehensive understanding of ozone formation during pollution episodes underscores the need for targeted and localized emission control measures, which has practical implications for implementation of effective emission control strategies. These findings help develop more precise and tailored approaches for improving air quality and reducing ozone pollution in the Houston area.

CRediT authorship contribution statement

Ehsan Soleimanian: Conceptualization, Methodology, Formal analysis, Data curation, Validation, Visualization, Writing – original draft. **Yuxuan Wang:** Conceptualization, Methodology, Validation, Funding acquisition, Project administration, Resources, Supervision, Writing – review & editing. **Wei Li:** Methodology, Formal analysis, Data curation. **Xueying Liu:** Methodology, Formal analysis, Data curation. **Travis Griggs:** Validation, Resources, Writing – review & editing. **James Flynn:** Validation, Resources, Writing – review & editing. **Paul J. Walter:** Validation, Resources, Supervision, Writing – review & editing. **Mark J. Estes:** Validation, Resources, Supervision, Writing – review & editing.

Declaration of competing interest

The authors declare that they have no known competing financial interests or personal relationships that could have appeared to influence the work reported in this paper.

Data availability

Data will be made available on request.

Acknowledgements

The authors wish to thank the financial support from the Texas Commission on Environmental Quality (Grant No. 582-22-31913-019

and 582-22-31913-020). The findings, opinions, and conclusions are the work of the author(s) and do not necessarily represent the findings, opinions, or conclusions of the TCEQ. Also, we would like to thank TCEQ for the air pollution monitoring system and providing surface levels of pollutants.

Appendix A. Supplementary data

Supplementary data to this article can be found online at <https://doi.org/10.1016/j.scitotenv.2023.165881>.

References

- Alvarado, L., Richter, A., Vrekoussis, M., Hilboll, A., Kalisz Hedegaard, A.B., Schneising, O., Burrows, J.P., 2020. Unexpected long-range transport of glyoxal and formaldehyde observed from the Copernicus Sentinel-5 precursor satellite during the 2018 Canadian wildfires. *Atmos. Chem. Phys.* 20, 2057–2072.
- Anenberg, S.C., West, J.J., Fiore, A.M., Jaffe, D.A., Prather, M.J., Bergmann, D., Cuvelier, K., Dentener, F.J., Duncan, B.N., Gauss, M., 2009. Intercontinental Impacts of Ozone Pollution on Human Mortality. *Auvray, M., Bey, I., 2005. Long-range transport to Europe: seasonal variations and implications for the European ozone budget. *J. Geophys. Res. Atmos.* 110.*
- Banta, R.M., Senff, C.J., Nielsen-Gammon, J., Darby, L.S., Ryerson, T.B., Alvarez, R.J., Sandberg, S.P., Williams, E.J., Trainer, M., 2005. A bad air day in Houston. *Bull. Am. Meteorol. Soc.* 86, 657–670.
- Beddows, A.V., Kitwiroon, N., Williams, M.L., Beevers, S.D., 2017. Emulation and sensitivity analysis of the community multiscale air quality model for a UK ozone pollution episode. *Environ. Sci. Technol.* 51, 6229–6236.
- Berezina, E., Moiseenko, K., Skorokhod, A., Pankratova, N.V., Belikov, I., Belousov, V., Elansky, N.F., 2020. Impact of VOCs and NOx on ozone formation in Moscow. *Atmosphere (Basel)* 11, 1262.
- Berkowitz, C.M., Jobson, T., Jiang, G., Spicer, C.W., Doskey, P.V., 2004. Chemical and meteorological characteristics associated with rapid increases of O₃ in Houston, Texas. *J. Geophys. Res. Atmos.* 109 (D10).
- Bernier, C., Wang, Y., Estes, M., Lei, R., Jia, B., Wang, S., Sun, J., 2019. Clustering surface ozone diurnal cycles to understand the impact of circulation patterns in Houston, TX. *J. Geophys. Res. Atmos.* 124, 13457–13474.
- Brioude, J., Arnold, D., Stohl, A., Cassiani, M., Morton, D., Seibert, P., Angevine, W., Evan, S., Dingwell, A., Fast, J.D., 2013. The Lagrangian particle dispersion model FLEXPART-WRF version 3.1. *Geosci. Model Dev.* 6, 1889–1904.
- Brown, S.S., Dubé, W.P., Bahreini, R., Middlebrook, A.M., Brock, C.A., Warneke, C., De Gouw, J.A., Washenfelder, R.A., Atlas, E., Peischl, J., 2013. Biogenic VOC oxidation and organic aerosol formation in an urban nocturnal boundary layer: aircraft vertical profiles in Houston, TX. *Atmos. Chem. Phys.* 13, 11317–11337.
- Buzcu, B., Fraser, M.P., 2006. Source identification and apportionment of volatile organic compounds in Houston, TX. *Atmos. Environ.* 40, 2385–2400.
- Byun, D.W., Kim, S.-T., Kim, S.-B., 2007. Evaluation of air quality models for the simulation of a high ozone episode in the Houston metropolitan area. *Atmos. Environ.* 41, 837–853.
- Camalier, L., Cox, W., Dolwick, P., 2007. The effects of meteorology on ozone in urban areas and their use in assessing ozone trends. *Atmos. Environ.* 41, 7127–7137.
- Chen, S., Brune, W.H., 2012. Global sensitivity analysis of ozone production and O₃-NO_x-VOC limitation based on field data. *Atmos. Environ.* 55, 288–296.
- Chen, F., Dudhia, J., 2001. Coupling an advanced land surface-hydrology model with the Penn State–NCAR MM5 modeling system. Part I: model implementation and sensitivity. *Mon. Weather Rev.* 129, 569–585.
- Chen, F., Janjić, Z., Mitchell, K., 1997. Impact of atmospheric surface-layer parameterizations in the new land-surface scheme of the NCEP mesoscale Eta model. *Boundary-Layer Meteorol.* 85, 391–421.
- Chen, W.T., Shao, M., Lu, S.H., Wang, M., Zeng, L.M., Yuan, B., Liu, Y., 2014. Understanding primary and secondary sources of ambient carbonyl compounds in Beijing using the PMF model. *Atmos. Chem. Phys.* 14, 3047–3062.
- Cowling, E.B., Furiness, C., Dimitriades, B., Parrish, D., 2007. Final rapid science synthesis report: findings from the second Texas air quality study (TexAQS II). *TCEQ Contract 65614.*
- Daly, A., Zannetti, P., 2007. Air pollution modeling—an overview. *Ambient Air Pollut.* 15–28.
- Darby, L.S., 2005. Cluster analysis of surface winds in Houston, Texas, and the impact of wind patterns on ozone. *J. Appl. Meteorol. Climatol.* 44, 1788–1806.
- De Gouw, J.A., Middlebrook, A.M., Warneke, C., Goldan, P.D., Kuster, W.C., Roberts, J. M., Fehsenfeld, F.C., Worsnop, D.R., Canagaratna, M.R., Pszenny, A.A.P., 2005. Budget of organic carbon in a polluted atmosphere: results from the New England Air Quality Study in 2002. *J. Geophys. Res. Atmos.* 110.
- DISCOVER-AQ, 2013. Deriving Information on Surface Conditions from Column and Vertically Resolved Observations Relevant to Air Quality.
- Draxler, R.R., Rolph, G.D., 2010. HYSPPLIT (HYbrid Single-Particle Lagrangian Integrated Trajectory) Model Access Via NOAA ARL READY Website (<http://ready.arl.noaa.gov/HYSPLIT.php>). NOAA Air Resources Laboratory, Silver Spring, MD, p. 25.
- Du, X., Tang, W., Cheng, M., Zhang, Z., Li, Yang, Li, Yu, Meng, F., 2022. Modeling of spatial and temporal variations of ozone-NO_x-VOC sensitivity based on photochemical indicators in China. *J. Environ. Sci.* 114, 454–464.

- Dunker, A.M., Wilson, G., Bates, J.T., Yarwood, G., 2020. Chemical sensitivity analysis and uncertainty analysis of ozone production in the comprehensive air quality model with extensions applied to Eastern Texas. *Environ. Sci. Technol.* 54, 5391–5399.
- Emanuel, K.A., Živković-Rothman, M., 1999. Development and evaluation of a convection scheme for use in climate models. *J. Atmos. Sci.* 56, 1766–1782.
- ENVIRON., 2020. User's Guide to the Comprehensive Air Quality Model with Extensions Version 7.10.
- Ericksen, L.E., Newmark, G.L., Higgins, M.J., Wang, Z., 2020. Nitrogen oxides and ozone in urban air: a review of 50 plus years of progress. *Environ. Prog. Sustain. Energy* 39, e13484.
- Fischer, E.V., Jacob, D.J., Yantosca, R.M., Sulprizio, M.P., Millet, D.B., Mao, J., Paulot, F., Singh, H.B., Roiger, A., Ries, L., 2014. Atmospheric peroxyacetyl nitrate (PAN): a global budget and source attribution. *Atmos. Chem. Phys.* 14, 2679–2698.
- Ge, S., Wang, S., Xu, Q., Ho, T., 2021a. Characterization and sensitivity analysis on ozone pollution over the Beaumont-Port Arthur Area in Texas of USA through source apportionment technologies. *Atmos. Res.* 247, 105249.
- Ge, S., Wang, S., Zhang, J., Xu, Q., Ho, T., 2021b. Ozone pollution control strategies examined by Empirical Kinetics Modeling Approach over the Beaumont-Port Arthur region in Texas of USA. *Atmos. Pollut. Res.* 12, 403–413.
- Giligan, J.M., Gutowski Jr., W.J., Cassano, J.J., Higgins, M.E., 2013. Effects of spectral nudging in WRF on Arctic temperature and precipitation simulations. *J. Clim.* 26, 3985–3999.
- Goldan, P.D., Kuster, W.C., Williams, E., Murphy, P.C., Fehsenfeld, F.C., Meagher, J., 2004. Nonmethane hydrocarbon and oxy hydrocarbon measurements during the 2002 New England Air Quality Study. *J. Geophys. Res. Atmos.* 109.
- Goldberg, D.L., Anenberg, S.C., Griffin, D., McLinden, C.A., Lu, Z., Streets, D.G., 2020. Disentangling the impact of the COVID-19 lockdowns on urban NO₂ from natural variability. *Geophys. Res. Lett.* 47, e2020GL089269.
- Gorai, A.K., Tulari, F., Tchounwou, P.B., Ambinakudige, S., 2015. Influence of local meteorology and NO₂ conditions on ground-level ozone concentrations in the eastern part of Texas, USA. *Air Qual. Atmos. Health* 8, 81–96.
- Grosjean, D., Grosjean, E., Williams, E.L., 1994. Thermal decomposition of PAN, PPN and vinyl-PAN. *Air Waste* 44, 391–396.
- Han, Y.-J., Holsten, T.M., Hopke, P.K., Yi, S.-M., 2005. Comparison between back-trajectory based modeling and Lagrangian backward dispersion modeling for locating sources of reactive gaseous mercury. *Environ. Sci. Technol.* 39, 1715–1723.
- Hanna, S.R., 1982. Applications in air pollution modeling. *Atmos. Turbul. Air Pollut. 275–310. Model. A Course held Hague, 21–25 Sept. 1981.*
- Heard, D.E., Pilling, M.J., 2003. Measurement of OH and HO₂ in the troposphere. *Chem. Rev.* 103, 5163–5198.
- Hearty, J., Draxler, R.R., Stein, A.F., Brioude, J., Mountain, M., Eluszkiewicz, J., Nehrkorn, T., Ngan, F., Andrews, A., 2013. Evaluation of Lagrangian particle dispersion models with measurements from controlled tracer releases. *J. Appl. Meteorol. Climatol.* 52, 2623–2637.
- Hidy, G.M., 2000. Ozone process insights from field experiments—part I: overview. *Atmos. Environ.* 34, 2001–2022.
- Holnicki, P., Nahorski, Z., 2015. Emission data uncertainty in urban air quality modeling—case study. *Environ. Model. Assess.* 20, 583–597.
- Huang, Z., Ou, J., Zheng, J., Yuan, Z., Yin, S., Chen, D., Tan, H., 2016. Process contributions to secondary inorganic aerosols during typical pollution episodes over the Pearl River Delta region, China. *Aerosol Air Qual. Res.* 16, 2129–2144.
- Iacono, M.J., Delamere, J.S., Mlawer, E.J., Shephard, M.W., Clough, S.A., Collins, W.D., 2008. Radiative forcing by long-lived greenhouse gases: calculations with the AER radiative transfer models. *J. Geophys. Res. Atmos.* 113.
- Jiménez, P., Baldasano, J.M., 2004. Ozone response to precursor controls in very complex terrains: Use of photochemical indicators to assess O₃-NO_x-VOC sensitivity in the northeastern Iberian Peninsula. *J. Geophys. Res. Atmos.* 109.
- Jorqueria, H., Rappenglück, B., 2004. Receptor modeling of ambient VOC at Santiago, Chile. *Atmos. Environ.* 38, 4243–4263.
- Kim, S.-W., McKeen, S.A., Frost, G.J., Lee, S.-H., Trainer, M., Richter, A., Angevine, W.M., Atlas, E., Bianco, L., Boersma, K.F., 2011. Evaluations of NO x and highly reactive VOC emission inventories in Texas and their implications for ozone plume simulations during the Texas Air Quality Study 2006. *Atmos. Chem. Phys.* 11, 11361–11386.
- Kleinman, L.I., 2005. The dependence of tropospheric ozone production rate on ozone precursors. *Atmos. Environ.* 39, 575–586.
- Kleinman, L.I., Daum, P.H., Lee, Y., Nunnermacker, L.J., Springston, S.R., Weinstein-Lloyd, J., Rudolph, J., 2001. Sensitivity of ozone production rate to ozone precursors. *Geophys. Res. Lett.* 28, 2903–2906.
- Kleinman, L.I., Daum, P.H., Imre, D., Lee, Y., Nunnermacker, L.J., Springston, S.R., Weinstein-Lloyd, J., Rudolph, J., 2002. Ozone production rate and hydrocarbon reactivity in 5 urban areas: a cause of high ozone concentration in Houston. *Geophys. Res. Lett.* 29, 101–105.
- Kleinman, L.I., Daum, P.H., Lee, Y., Nunnermacker, L.J., Springston, S.R., Weinstein-Lloyd, J., Rudolph, J., 2005. A comparative study of ozone production in five US metropolitan areas. *J. Geophys. Res. Atmos.* 110.
- Kotsakis, A., Sullivan, J.T., Hanisco, T.F., Swap, R.J., Caicedo, V., Berkoff, T.A., Gronoff, G., Loughner, C.P., Ren, X., Luke, W.T., 2022. Sensitivity of total column NO₂ at a marine site within the Chesapeake Bay during OWLETS-2. *Atmos. Environ.* 277, 119063.
- Krüger, B.C., Katragkou, E., Tegoulias, I., Zanis, P., Melas, D., Coppola, E., Rauscher, S., Huszar, P., Halenka, T., 2008. Regional photochemical model calculations for Europe concerning ozone levels in a changing climate. *Időjáras* 112, 285–300.
- Langford, A.O., Senff, C.J., Banta, R.M., Hardesty, R.M., Alvarez, R.J., Sandberg, S.P., Darby, L.S., 2009. Regional and local background ozone in Houston during Texas Air Quality Study 2006. *J. Geophys. Res. Atmos.* 114.
- Latto, A., Hagen, A., Berg, R., 2021. National Hurricane Center Tropical Cyclone Report. *Hurric. Isaías 1–32.*
- Lefohn, A.S., Malley, C.S., Smith, L., Wells, B., Hazucha, M., Simon, H., Naik, V., Mills, G., Schultz, M.G., Paoletti, E., 2018. Tropospheric ozone assessment report: global ozone metrics for climate change, human health, and crop/ecosystem research. *Elem. Sci. Anthr.* 6.
- Lei, W., Zhang, R., Tie, X., Hess, P., 2004. Chemical characterization of ozone formation in the Houston-Galveston area: a chemical transport model study. *J. Geophys. Res. Atmos.* 109.
- Leuchner, M., Rappenglück, B., 2010. VOC source-receptor relationships in Houston during TexAQS-II. *Atmos. Environ.* 44, 4056–4067.
- Lew, M.M., Ricky, P.S., Bottorff, B.P., Reidy, E., Sklavenniti, S., Léonardis, T., Locoge, N., Dusante, S., Kundu, S., Wood, E., 2020. OH and HO 2 radical chemistry in a midlatitude forest: measurements and model comparisons. *Atmos. Chem. Phys.* 20, 9209–9230.
- Li, G., Zhang, R., Fan, J., Tie, X., 2007. Impacts of biogenic emissions on photochemical ozone production in Houston, Texas. *J. Geophys. Res. Atmos.* 112.
- Li, Y., Lau, A., Fung, J., Zheng, J.Y., Zhong, L.J., Louie, P.K.K., 2012. Ozone source apportionment (OSAT) to differentiate local regional and super-regional source contributions in the Pearl River Delta region, China. *J. Geophys. Res. Atmos.* 117.
- Li, L., Xie, S., Zeng, L., Wu, R., Li, J., 2015. Characteristics of volatile organic compounds and their role in ground-level ozone formation in the Beijing-Tianjin-Hebei region, China. *Atmos. Environ.* 113, 247–254.
- Li, L., An, J.Y., Shi, Y.Y., Zhou, M., Yan, R.S., Huang, C., Wang, H.L., Lou, S.R., Wang, Q., Lu, Q., 2016. Source apportionment of surface ozone in the Yangtze River Delta, China in the summer of 2013. *Atmos. Environ.* 144, 194–207.
- Li, L., An, J., Huang, L., Yan, R., Huang, C., Yarwood, G., 2019. Ozone source apportionment over the Yangtze River Delta region, China: investigation of regional transport, sectoral contributions and seasonal differences. *Atmos. Environ.* 202, 269–280.
- Li, W., Wang, Y., Bernier, C., Estes, M., 2020. Identification of sea breeze recirculation and its effects on ozone in Houston, TX, during DISCOVER-AQ 2013. *J. Geophys. Res. Atmos.* 125, e2020JD033165.
- Li, W., Wang, Y., Liu, X., Soleimanian, E., Griggs, T., Flynn, J., Walter, P., 2023. Understanding offshore high-ozone events during TRACER-AQ 2021 in Houston: insights from WRR-CAMx photochemical modeling. *Egusph. <https://doi.org/10.5194/egusphere-2023-1117> [preprint].*
- Liu, P., Tsimpidi, A.P., Hu, Y., Stone, B., Russell, A.G., Nenes, A., 2012. Differences between downscaling with spectral and grid nudging using WRF. *Atmos. Chem. Phys.* 12, 3601–3610.
- Liu, L., Talbot, R., Lan, X., 2015. Influence of climate change and meteorological factors on Houston's air pollution: ozone a case study. *Atmosphere (Basel)* 6, 623–640.
- Liu, X., Wang, Y., Wasti, S., Li, W., Soleimanian, E., Flynn, J., Griggs, T., Alvarez, S., Sullivan, J.T., Roots, M., Twigg, L., Gronoff, G., Berkoff, T., Walter, P., Estes, M., Hair, J.W., Shingler, T., Scarino, A.J., Fenn, M., Judd, L., 2023. Evaluating WRF-GC predictions of boundary layer and vertical ozone profiles during the 2021 TRACER-AQ campaign in Houston, Texas. *Egusph. [preprint]. <https://doi.org/10.5194/egusphere-2023-892>.*
- Loughner, C.P., Allen, D.J., Pickering, K.E., Zhang, D.-L., Shou, Y.-X., Dickerson, R.R., 2011. Impact of fair-weather cumulus clouds and the Chesapeake Bay breeze on pollutant transport and transformation. *Atmos. Environ.* 45, 4060–4072.
- Loughner, C.P., Tzortziou, M., Follette-Cook, M., Pickering, K.E., Goldberg, D., Satam, C., Weinheimer, A., Crawford, J.H., Knapp, D.J., Montzka, D.D., 2014. Impact of bay-breeze circulations on surface air quality and boundary layer export. *J. Appl. Meteorol. Climatol.* 53, 1697–1713.
- Lu, X., Zhang, L., Shen, L., 2019. Meteorology and climate influences on tropospheric ozone: a review of natural sources, chemistry, and transport patterns. *Curr. Pollut. Rep.* 5, 238–260.
- Ma, Y., Fu, S., Gao, S., Zhang, S., Che, X., Wang, Q., Jiao, Z., 2021. Update on volatile organic compound (VOC) source profiles and ozone formation potential in synthetic resins industry in China. *Environ. Pollut.* 291, 118253.
- Mazzuca, G.M., Ren, X., Loughner, C.P., Estes, M., Crawford, J.H., Pickering, K.E., Weinheimer, A.J., Dickerson, R.R., 2016. Ozone production and its sensitivity to NO x and VOCs: results from the DISCOVER-AQ field experiment, Houston 2013. *Atmos. Chem. Phys.* 16, 14463–14474.
- Mazzuca, G.M., Pickering, K.E., Clark, R.D., Loughner, C.P., Fried, A., Zweers, D.C.S., Weinheimer, A.J., Dickerson, R.R., 2017. Use of tethersonde and aircraft profiles to study the impact of mesoscale and microscale meteorology on air quality. *Atmos. Environ.* 149, 55–69.
- Morris, G.A., Hersey, S., Thompson, A.M., Pawson, S., Nielsen, J.E., Colarco, P.R., McMillan, W.W., Stohl, A., Turquety, S., Warner, J., 2006. Alaskan and Canadian forest fires exacerbate ozone pollution over Houston, Texas, on 19 and 20 July 2004. *J. Geophys. Res. Atmos.* 111.
- Morris, G.A., Ford, B., Rappenglück, B., Thompson, A.M., Mefferd, A., Ngan, F., Lefer, B., 2010. An evaluation of the interaction of morning residual layer and afternoon mixed layer ozone in Houston using ozonesonde data. *Atmos. Environ.* 44, 4024–4034.
- Morrison, H., Thompson, G., Tatarki, V., 2009. Impact of cloud microphysics on the development of trailing stratiform precipitation in a simulated squall line: comparison of one-and two-moment schemes. *Mon. Weather Rev.* 137, 991–1007.
- Nakanishi, M., Niino, H., 2009. Development of an improved turbulence closure model for the atmospheric boundary layer. *J. Meteorol. Soc. Japan. Ser. II* 87, 895–912.
- Nuvolone, D., Petri, D., Voller, F., 2018. The effects of ozone on human health. *Environ. Sci. Pollut. Res.* 25, 8074–8088.

- Owen, R.C., Honrath, R.E., 2009. A new method for the Lagrangian tracking of pollution plumes from source to receptor using gridded model output. *Atmos. Chem. Phys.* 9, 2577–2595.
- Pan, S., Choi, Y., Roy, A., Li, X., Jeon, W., Souri, A.H., 2015. Modeling the uncertainty of several VOC and its impact on simulated VOC and ozone in Houston, Texas. *Atmos. Environ.* 120, 404–416.
- Pirovano, G., Coll, I., Bedogni, M., Alessandrini, S., Costa, M.P., Gabusi, V., Lasry, F., Menut, L., Vautard, R., 2007. On the influence of meteorological input on photochemical modelling of a severe episode over a coastal area. *Atmos. Environ.* 41, 6445–6464.
- Pisso, I., Sollum, E., Grythe, H., Kristiansen, N.I., Cassiani, M., Eckhardt, S., Arnold, D., Morton, D., Thompson, R.L., Groot Zwaaftink, C.D., 2019. The Lagrangian particle dispersion model FLEXPART version 10.4. *Geosci. Model Dev.* 12, 4955–4997.
- Rao, K.S., 2005. Uncertainty analysis in atmospheric dispersion modeling. *Pure Appl. Geophys.* 162, 1893–1917.
- Register, F., 2015. 80 FR 65292-National Ambient Air Quality Standards for Ozone (2015), pp. 65292–65468.
- Ren, X., Van Duin, D., Cazorla, M., Chen, S., Mao, J., Zhang, L., Brune, W.H., Flynn, J.H., Grossberg, N., Lefer, B.L., 2013. Atmospheric oxidation chemistry and ozone production: results from SHARP 2009 in Houston, Texas. *J. Geophys. Res. Atmos.* 118, 5770–5780.
- Sharma, S., Sharma, P., Khare, M., 2017. Photo-chemical transport modelling of tropospheric ozone: a review. *Atmos. Environ.* 159, 34–54.
- Shen, J., Wang, X., Li, J., Li, Y., Zhang, Y., 2011. Evaluation and intercomparison of ozone simulations by Models-3/CMAQ and CAMx over the Pearl River Delta. *Sci. China Chem.* 54, 1789–1800.
- Shu, Q., Napelenok, S.L., Hutzell, W.T., Baker, K.R., Henderson, B.H., Murphy, B.N., Hogrefe, C., 2023. Comparison of ozone formation attribution techniques in the northeastern United States. *Geosci. Model Dev.* 16, 2303–2322.
- Sillman, S., 1995. The use of NO_y, H₂O₂, and HNO₃ as indicators for ozone-NO-x hydrocarbon sensitivity in urban locations. *J. Geophys. Res. Atmos.* 100, 14175–14188.
- Skamarock, W.C., Klemp, J.B., Dudhia, J., Gill, D.O., Barker, D.M., Wang, W., Powers, J.G., 2008. A Description of the Advanced Research WRF version 3. NCAR Technical Note-475+ STR.
- Skamarock, W.C., Klemp, J.B., Dudhia, J., Gill, D.O., Liu, Z., Berner, J., Wang, W., Powers, J.G., Duda, M.G., Barker, D.M., 2019. A Description of the Advanced Research WRF Model Version 4, 145. Natl. Cent. Atmos. Res., Boulder, CO, USA, p. 145.
- Soleimanian, E., Wang, Y., Estes, M., 2022. Long-term trend in surface ozone in Houston-Galveston-Brazoria: sectoral contributions based on changes in volatile organic compounds. *Environ. Pollut.* 308, 119647.
- Srinivas, C.V., Hari Prasad, K., Naidu, C.V., Baskaran, R., Venkatraman, B., 2016. Sensitivity analysis of atmospheric dispersion simulations by FLEXPART to the WRF-simulated meteorological predictions in a coastal environment. *Pure Appl. Geophys.* 173, 675–700.
- Stein, A.F., Draxler, R.R., Rolph, G.D., Stunder, B.J.B., Cohen, M.D., Ngan, F., 2015. NOAA's HYSPLIT atmospheric transport and dispersion modeling system. *Bull. Am. Meteorol. Soc.* 96, 2059–2077.
- Stohl, A., Hittenberger, M., Wotawa, G., 1998. Validation of the Lagrangian particle dispersion model FLEXPART against large-scale tracer experiment data. *Atmos. Environ.* 32, 4245–4264.
- Stohl, A., Forster, C., Frank, A., Seibert, P., Wotawa, G., 2005. The Lagrangian particle dispersion model FLEXPART version 6.2. *Atmos. Chem. Phys.* 5, 2461–2474.
- Tan, Z., Lu, K., Dong, H., Hu, M., Li, X., Liu, Y., Lu, S., Shao, M., Su, R., Wang, H., 2018. Explicit diagnosis of the local ozone production rate and the ozone-NOx-VOC sensitivities. *Sci. Bull.* 63, 1067–1076.
- TexAQS, 2000. Texas Air Quality Study, a Photochemical Oxidant and Aerosol Field Program [WWW Document].
- TexAQS, I.I., 2006. Texas Air Quality Study II - Gulf of Mexico Atmospheric Composition and Climate Study [WWW Document].
- Tiedtke, M., 1989. A comprehensive mass flux scheme for cumulus parameterization in large-scale models. *Mon. Weather Rev.* 117, 1779–1800.
- Vermeuel, M.P., Novak, G.A., Alwe, H.D., Hughes, D.D., Kaleel, R., Dickens, A.F., Kenski, D., Czarnetzki, A.C., Stone, E.A., Stanier, C.O., 2019. Sensitivity of ozone production to NO_x and VOC along the Lake Michigan coastline. *J. Geophys. Res. Atmos.* 124, 10989–11006.
- Verreyken, B., Brioude, J., Evan, S., 2019. Development of turbulent scheme in the FLEXPART-AROME v1. 2.1 Lagrangian particle dispersion model. *Geosci. Model Dev.* 12, 4245–4259.
- Vizuete, W., Kim, B.-U., Jeffries, H., Kimura, Y., Allen, D.T., Kioumourtzoglou, M.-A., Biton, L., Henderson, B., 2008. Modeling ozone formation from industrial emission events in Houston, Texas. *Atmos. Environ.* 42, 7641–7650.
- Wang, X., Li, J., Zhang, Y., Xie, S., Tang, X., 2009. Ozone source attribution during a severe photochemical smog episode in Beijing, China. *Sci. China Ser. B Chem.* 52, 1270–1280.
- Wang, H.K., Huang, C.H., Chen, K.S., Peng, Y.P., 2010a. Seasonal variation and source apportionment of atmospheric carbonyl compounds in urban Kaohsiung, Taiwan. *Aerosol Air Qual. Res.* 10, 559–570.
- Wang, X., Zhang, Y., Hu, Y., Zhou, W., Lu, K., Zhong, L., Zeng, L., Shao, M., Hu, M., Russell, A.G., 2010b. Process analysis and sensitivity study of regional ozone formation over the Pearl River Delta, China, during the PRIDE-PRD2004 campaign using the Community Multiscale Air Quality modeling system. *Atmos. Chem. Phys.* 10, 4423–4437.
- Wang, Y., Jia, B., Wang, S.-C., Estes, M., Shen, L., Xie, Y., 2016. Influence of the Bermuda High on interannual variability of summertime ozone in the Houston-Galveston-Brazoria region. *Atmos. Chem. Phys.* 16, 15265–15276.
- Wang, T., Xue, L., Brimblecombe, P., Lam, Y.F., Li, L., Zhang, L., 2017. Ozone pollution in China: a review of concentrations, meteorological influences, chemical precursors, and effects. *Sci. Total Environ.* 575, 1582–1596.
- Ward Jr., J.H., 1963. Hierarchical grouping to optimize an objective function. *J. Am. Stat. Assoc.* 58, 236–244.
- Webster, M., Nam, J., Kimura, Y., Jeffries, H., Vizuete, W., Allen, D.T., 2007. The effect of variability in industrial emissions on ozone formation in Houston, Texas. *Atmos. Environ.* 41, 9580–9593.
- Wu, W., Xue, W., Zheng, Y., Wang, Y., Lei, Y., Wang, J., 2021. Diurnal regulation of VOCs may not be effective in controlling ozone pollution in China. *Atmos. Environ.* 256, 118442.
- Xie, Y., Berkowitz, C.M., 2006. The use of positive matrix factorization with conditional probability functions in air quality studies: an application to hydrocarbon emissions in Houston, Texas. *Atmos. Environ.* 40, 3070–3091.
- Xue, L.K., Wang, T., Gao, J., Ding, A.J., Zhou, X.H., Blake, D.R., Wang, X.F., Saunders, S. M., Fan, S.J., Zuo, H.C., 2014. Ground-level ozone in four Chinese cities: precursors, regional transport and heterogeneous processes. *Atmos. Chem. Phys.* 14, 13175–13188.
- Yang, L., Luo, H., Yuan, Z., Zheng, J., Huang, Z., Li, C., Lin, X., Louie, P.K.K., Chen, D., Bian, Y., 2019. Quantitative impacts of meteorology and precursor emission changes on the long-term trend of ambient ozone over the Pearl River Delta, China, and implications for ozone control strategy. *Atmos. Chem. Phys.* 19, 12901–12916.
- Ying, Q., Krishnan, A., 2010. Source contributions of volatile organic compounds to ozone formation in southeast Texas. *J. Geophys. Res. Atmos.* 115.
- Zannetti, P., 2013. Air Pollution Modeling: Theories, Computational Methods and Available Software. Springer Science & Business Media.
- Zhang, R., Lei, W., Tie, X., Hess, P., 2004. Industrial emissions cause extreme urban ozone diurnal variability. *Proc. Natl. Acad. Sci.* 101, 6346–6350.
- Zhang, C., Wang, Y., Hamilton, K., 2011. Improved representation of boundary layer clouds over the southeast Pacific in ARW-WRF using a modified Tiedtke cumulus parameterization scheme. *Mon. Weather Rev.* 139, 3489–3513.
- Zhang, B., Owen, R.C., Perlinger, J.A., Kumar, A., Wu, S., Val Martin, M., Kramer, L., Helmig, D., Honrath, R.E., 2014. A semi-Lagrangian view of ozone production tendency in north American outflow in the summers of 2009 and 2010. *Atmos. Chem. Phys.* 14, 2267–2287.
- Zhang, R., Cohan, A., Bazar, A.P., Cohan, D.S., 2017. Source apportionment of biogenic contributions to ozone formation over the United States. *Atmos. Environ.* 164, 8–19.
- Zhang, G., Jing, S., Xu, W., Gao, Y., Yan, C., Liang, L., Huang, C., Wang, H., 2021. Simultaneous observation of atmospheric peroxyacetyl nitrate and ozone in the megacity of Shanghai, China: regional transport and thermal decomposition. *Environ. Pollut.* 274, 116570.
- Zhao, K., Wu, Y., Yuan, Z., Huang, J., Liu, X., Ma, W., Xu, D., Jiang, R., Duan, Y., Fu, Q., 2022. Understanding the underlying mechanisms governing the linkage between atmospheric oxidative capacity and ozone precursor sensitivity in the Yangtze River Delta, China: a multi-tool ensemble analysis. *Environ. Int.* 160, 107060.
- Zhou, W., Cohan, D.S., Henderson, B.H., 2014. Slower ozone production in Houston, Texas following emission reductions: evidence from Texas Air Quality Studies in 2000 and 2006. *Atmos. Chem. Phys.* 14, 2777–2788.